Cytoplasmic mRNA decay by the anti-viral nuclease RNase L promotes transcriptional repression

Xiaowen Mao[1], Sherzod Tokamov[1], Felix Pahmeier[2], Azra Lari[1], Jinyi Xu[3], Eva Harris[2], Britt Glaunsinger[1,3,4*]

[1] Department of Plant and Microbial Biology, UC Berkeley, Berkeley, CA, USA

[2] Division of Infectious Diseases and Vaccinology, School of Public Health, University of California, Berkeley, Berkeley, CA, USA

[3] Department of Molecular and Cell Biology, UC Berkeley, Berkeley, CA, USA

[4] Howard Hughes Medical Institute, UC Berkeley, CA, USA

*To whom correspondence may be addressed. Email: glaunsinger@berkeley.edu

SUMMARY

Ribonuclease (RNase) L is an antiviral factor that promiscuously degrades viral and cellular RNA in the cytoplasm. This results in extensive translational reprogramming, altering mRNA processing and export. Here, we reveal that another major consequence of cytoplasmic RNase L activity is the repression of nascent RNA synthesis in the nucleus. This is not associated with altered nuclear RNA stability but instead results from transcriptional repression. For RNA polymerase II, repression is primarily associated with reduced occupancy of serine 2-phosphorylated polymerase in gene bodies, indicating an elongation defect. Prominent among the transcriptionally downregulated loci are immune-related genes, supporting a role for RNase L in tempering innate immune and inflammatory responses. RNase L activation also caused disruption of nucleoli and reduced RNA polymerase I and III transcription. Crosstalk between RNA decay and transcription thereby contributes to the large-scale modulation of gene expression in RNase L-activated cells.

27 # Introduction

28 Ribonuclease (RNase) L is an important player in the innate immune response triggered by
29 double-stranded RNA (dsRNA), a pathogen-associated molecular pattern (PAMP) commonly
30 associated with viral infections. RNase L dimerizes and is activated by 2'-5'-oligo(A), a
31 second messenger produced by the oligoadenylate synthetases (OAS) 1-3 upon dsRNA
32 binding. Once activated, RNase L promiscuously cleaves cytoplasmic RNA, including viral
33 RNAs and host rRNA, mRNA, and tRNA, at sites defined by UN^N [1]. RNase L was initially
34 hypothesized to suppress translation through its ability to cleave rRNA and tRNA. However,
35 rRNA and tRNA cleavage occurs after translation remodeling, and ribosomes with RNase L-
36 cleaved rRNAs can still support translation [2-4]. Thus, widespread cleavage of mRNA most
37 likely causes the prominent decrease in cellular translation [2,4,5].

38 In addition to suppressing viral gene expression, RNase L-induced gene expression
39 reprogramming both positively and negatively modulates innate immune responses [2,4-12].
40 RNAse L promotes virus-induced IFNβ production in mice and in cells where RNase L basal
41 expression is low, but suppresses IFNβ production in cells with higher basal RNase L and
42 OAS expression, perhaps to promote tissue protection [10,13]. Additionally, loss-of-function
43 mutations in the OAS-RNase L pathway have been linked to autoimmune diseases, including
44 some cases of multisystem inflammatory syndrome in children following SARS-CoV-2
45 infection [9]. These observations suggest that RNase L activity may dampen immune gene
46 expression to prevent overactivation of the innate immune system. However, some mRNAs
47 encoding antiviral factors are at least partially resistant to RNase L and may be preferentially
48 translated due to the liberated translational resources, ensuring the execution of an antiviral
49 response [2,4,5]. Much remains to be learned about the contexts governing the complex roles
50 of RNase L in immune regulation.

51 While RNA cleavage is a prominent phenotype associated with RNase L, several recent
52 findings reveal additional mechanisms contributing to its impact on gene expression. These
53 include inhibiting mRNA export [6], altering mRNA processing [7], activating ribotoxic stress
54 responses [8,11,14], and activating RIG-I/MDA5-MAVS pathways through the production of small

55 RNA cleavage fragments [10,13]. Each of these phenotypes relies on RNase L catalytic activity,
56 suggesting that they occur in response to the widespread RNA cleavage.

57 Several oncogenic gamma-herpesviruses also engage broad-acting mRNA-targeting
58 nucleases, whose activity, like that of RNase L, can lead to alterations in mRNA processing
59 and export [15-18]. Notably, viral cleavage of cytoplasmic mRNA also induces large-scale
60 dampening of RNA polymerase II (Pol II) transcription [19-21]. Similarly, widespread cytoplasmic
61 mRNA decay by the cellular exonuclease polyribonucleotide nucleotidyltransferase 1
62 (PNPT1), which is activated during early apoptosis, leads to subsequent Pol II transcriptional
63 repression [22-24]. These findings indicate that there is a positive feedback loop between mRNA
64 synthesis and degradation under conditions of accelerated mRNA decay, which we
65 hypothesized might also occur in response to RNase L activation.

66 Here, we reveal that activated RNase L represses RNA synthesis. This includes interferon-
67 stimulated genes and other immune genes, suggesting that its impact on RNA biogenesis
68 may help temper inflammatory responses. The reduction of newly synthesized RNA is not
69 due to accelerated RNA decay in the nucleus but instead is triggered indirectly by RNase L-
70 induced RNA degradation in the cytoplasm. This causes a reduction in transcription by Pol I,
71 II, and III, accompanied by alterations in nucleolar and nuclear speckle morphology. The
72 primary alteration to Pol II occupancy is a reduction in the serine 2-phosphorylated version
73 in the gene body and near transcription termination sites, suggestive of an elongation defect.
74 The repressive signal involves the transport of proteins into the nucleus, as blocking importin
75 β-mediated nuclear import rescues RNA synthesis in cells with activated RNase L. Thus,
76 crosstalk between the cytoplasm and nucleus promotes broad transcriptional repression
77 upon RNase L activation, which contributes to the reshaping of the gene expression
78 landscape in cells following innate immune stimulation.

79

80 **Results**

81 **RNase L activation broadly reduces the abundance of newly synthesized RNA in the**
82 **nucleus**

83 Based on observations of positive feedback between RNA decay and synthesis [19,24], we
84 sought to determine how RNase L impacts the abundance of newly synthesized RNA in the
85 nucleus. We first designed an assay to quantify the total pool of newly transcribed RNA in
86 response to RNase L activation. We activated RNase L by transfecting human A549 cells with
87 the double-stranded RNA mimic poly(I:C) for 4 hours, then added the uridine analog ethynyl
88 uridine (EU) for 30 minutes to label nascent transcripts. The EU-containing RNA was coupled
89 to a Cy5 fluorophore by click chemistry and then visualized by flow cytometry or imaging
90 (Figure 1A). We confirmed that the labeled RNA remained largely nuclear during the 30-
91 minute pulse (Figure S1A-B), which is important because, upon export to the cytoplasm,
92 RNA is rapidly degraded by RNase L.

93 We observed a striking reduction in EU incorporation in poly(I:C)-treated WT A549 cells
94 compared to control mock-treated cells (Figure 1B, C). In contrast, poly(I:C) treatment of
95 RNase L knock-out (RLKO) A549 cells resulted in only a modest reduction in EU signal (Figure
96 1B, C), suggesting that RNase L is the primary driver of the loss of newly transcribed RNA in
97 the nucleus. Furthermore, nascent RNA depletion was observed in A549 RLKO cells
98 complemented with WT RNase L but not those complemented with a catalytically dead
99 RNase L mutant R667A (Figure 1B, C), indicating that this effect required RNase L catalytic
100 activity. This phenotype was detected as early as 2 hours after poly(I:C) treatment and grew
101 progressively more pronounced over time (Figure S1C). It was also apparent in WT but not
102 RLKO cells treated with a synthetic version of the RNase L-activating second messenger
103 molecule 2-5A ($pA(_{2\text{-}5}A)_4$) (Figure S1D). Poly(I:C) transfection also reduced the EU signal in
104 immortalized murine bone marrow-derived macrophages (iBMDM), and this effect was
105 mitigated upon siRNA-mediated depletion of RNase L (Figure S1E-G). Although RNase L
106 activation can induce caspase-dependent apoptosis [12,25], the irreversible pan-caspase
107 inhibitor z-VAD(Ome)-FMK did not prevent the loss of EU signal (Figure S1H), indicating that
108 repression of nascent RNA does not require caspase activation.

109 To determine whether these observations occur during viral infection, we performed a 30-
110 minute EU pulse during Zika virus infection, which is a potent activator of RNase L [26-28].
111 Indeed, Zika virus infection at an MOI of 5 for 24 hours resulted in a significant reduction in
112 EU-labeled RNA in WT A549 cells compared to RLKO cells, as visualized by
113 immunofluorescence (Figure 1D-E, S1I). A portion of the Zika virus-induced reduction in
114 nascent RNA was RNase L-independent (Figure 1E), which may stem from other effects
115 induced by dsRNA and/or Zika virus capsid protein [29]. Collectively, these data indicate that
116 RNase L-mediated mRNA degradation represses nascent RNA synthesis in multiple cell
117 types and in response to multiple activating stimuli.

118

119 **RNase L reduces both nascent rRNA and pre-mRNA accumulation**

120 EU is incorporated into transcripts by all three classes of RNA polymerases, with RNA
121 polymerase I (Pol I) and Pol II transcripts each accounting for approximately half of the total
122 signal during a short pulse [30]. Thus, the loss in EU signal caused by RNase L activation is likely
123 due to the reduction of both nascent Pol I and Pol II transcripts. To comprehensively
124 investigate the nascent transcripts affected by RNase L activation, we sequenced the newly
125 transcribed pool of RNA following a 10-minute pulse labeling with another uridine analog, 4-
126 thiouridine (4sU). After adding labeled and unlabeled spike-in controls for normalization, the
127 4sU-incorporated RNA was purified away from the pre-existing pool of RNA by biotinylation
128 of the 4sU and purification via streptavidin beads (Figure 2A). We confirmed >30-fold
129 enrichment of the 4sU-labeled over the unlabeled spike-in RNA in our sequencing data and
130 confirmed 4sU RNA enrichment by RT-qPCR (Figure S2A-B).

131 Initial rRNA filtering revealed that the rRNA reads accounted for no more than 56% of the
132 total reads, which aligns with expectations [31]. After alignment to the rDNA repeat and spike-
133 in normalization, we observed a decrease in 4sU-seq signal coverage on the entire rDNA
134 repeat in WT cells transfected with poly(I:C), which was less prominent in RLKO cells (Figure
135 2B). We then aligned the remaining reads to the hg38 reference genome and performed a
136 metagene analysis on protein-coding genes. In agreement with the EU flow cytometry data,

137 we observed a global decrease in nascent mRNA transcripts in poly(I:C) treated WT cells
138 relative to mock treated WT cells, as well as in WT cells treated with poly(I:C) compared to
139 RLKO cells treated with poly(I:C) (Figure 2C). We also observed a prominent decrease in
140 several Pol III-transcribed genes (Figure S2C). Differential gene expression analysis of
141 protein-coding and non-coding genes transcribed by all three RNA polymerases revealed a
142 widespread decrease on a gene-by-gene basis, with 36.2% of genes significantly
143 downregulated (Figure 2D). Thus, RNase L plays a major role in repressing the accumulation
144 of nascent rRNA, noncoding RNA, and mRNA.

145 Fewer genes were significantly upregulated in an RNase L-dependent manner, and manual
146 inspection of these genes revealed that their apparent upregulation is largely explained by
147 one of two situations. The first category contains genes that are differentially expressed in
148 these cells even in the absence of poly(I:C) treatment, indicating they are the result of minor
149 genetic/epigenetic differences between the parental WT cell line and the clonal RLKO cell
150 line (Figure S2D-E). The second category includes genes whose apparent upregulation is
151 instead the result of read-through transcription from upstream highly expressed genes
152 (Figure S2F). Thus, RNase L activation predominantly causes repression rather than
153 activation of nascent RNA.

154 Notably, gene ontology analysis of the downregulated genes revealed an enrichment of
155 genes involved in cytoplasmic translation and the immune response (Figure 2E-F). The
156 translation term is likely due to the reduction in ribosomal protein-encoding mRNAs, which
157 are known targets of RNase L [32], suggesting a coordinated response with rRNA transcription
158 inhibition to reduce ribosome biogenesis [33]. The abundance of immune-related categories
159 suggests that RNase L-induced suppression of nascent RNA contributes to its impact on the
160 immune response. We validated this result by performing RT-qPCR on selected immune
161 transcripts in total RNA samples using intron-exon spanning primer pairs to measure pre-
162 mRNA. Indeed, interferon-stimulated genes (ISGs), including IFIT1, RSAD2, OAS1, and OASL,
163 displayed decreased pre-mRNA levels in WT cells compared to RLKO cells stimulated with
164 poly(I:C) (Figure 2G, S2G). In contrast, IFNL1 has previously been shown to undergo intron

165 retention upon RNase L activation, and we observed this expected increase (and a similar
166 trend for ISG15) in WT relative to RLKO cells (Figure 2G).

167 We next considered the extent to which the decrease in ISG pre-mRNA was due to a
168 reduction in interferon (IFN) signal amplification versus a cell-autonomous effect, as we
169 observed decreased levels of both nascent IFNB1 and IFNL1. This is also relevant because
170 degradation and/or export inhibition of interferons and other cytokine cytoplasmic mRNA by
171 RNase L should reduce the level of their encoded secreted proteins, thereby dampening
172 their ability to induce ISG expression in neighboring cells via paracrine signaling. To evaluate
173 this for ISGs, we treated cells concurrently with poly(I:C) and brefeldin A (BFA), which
174 collapses Golgi-ER retrograde transport and inhibits protein secretion [34]. BFA reduced the
175 difference in nascent mRNA levels between WT and RLKO cells for most of the ISGs we
176 tested, including IFIT1, RSAD2, OAS1, and OASL, confirming the impact of RNase L activity
177 on signal amplification of the interferon pathway (Figure 2G, S2G). However, the difference
178 in IL1A nascent mRNA levels between WT and RLKO cells remained upon BFA treatment
179 (Figure 2G), suggesting that the repression of nascent RNA can independently influence
180 some immune genes in a cell-autonomous manner.

181 **Reduction of nascent RNA is not due to accelerated nuclear RNA degradation**

182 RNase L is primarily described as a cytoplasmic nuclease [7,35]; however, even a small amount
183 of active RNase L in the nucleus could lead to rapid depletion of pre-mRNA. To directly test
184 whether RNase L activation increases degradation of nascent RNA in the nucleus, we
185 measured nascent RNA turnover using an EU pulse chase experiment. We pulsed poly(I:C)-
186 transfected cells with EU 1 hour after transfection, a time point when EU incorporation is
187 minimally affected by RNase L activation (Figure S1C, S3A). We then chased with excess
188 uridine over a 3-hour time course and measured the decay of the labeled RNA. Notably, the
189 rate of RNA decay was similar in A549 WT and A549 RLKO cells, indicating that RNase L does
190 not accelerate nascent RNA decay in the nucleus (Figure 3A). We confirmed that the
191 transfection conditions were sufficient to induce RNase L-specific reduction of nascent RNA

192 (Figure S3A-B, see the "pulse last" sample) and that our measurements largely captured
193 nuclear RNA (Figure S3C-D).

194 As an orthogonal way of confirming that the cytoplasmic fraction of RNase L is sufficient to
195 reduce nascent RNA in the nucleus, we complemented the RNase L knockout cells with a
196 Halo-tagged version of RNase L fused to a cytoplasmic retention signal (CRS) (Figure 3B)
197 derived from GDOWN1 (amino acid 250-368) [36]. This CRS promotes cytoplasmic retention
198 by both CRM1-dependent and -independent mechanisms and is strong enough to retain
199 HaloTag containing an SV40 nuclear localization signal within the cytoplasm (Figure S3E). As
200 expected, both CRS-Halo-RNase L and Halo-RNase L appeared restricted to the cytoplasm
201 (Figure 3C-E). Furthermore, both constructs reduced EU pulse-labeled nascent RNA levels
202 to a similar extent upon poly(I:C) transfection (Figure 3F-I), indicating that cytoplasmic
203 RNase L is sufficient to reduce nascent RNA in the nucleus. In contrast, cells overexpressing
204 CRS-Halo-NLS, a negative control, did not exhibit this pattern (Figure 3F, I). Taken together,
205 these data suggest that activated RNase L does not induce nuclear RNA decay but rather
206 reduces nascent RNA by affecting transcription.

207

208 **RNase L disrupts nucleoli and reduces serine-5-phosphorylated (S5P) Pol II levels in the**
209 **nucleus**

210 We first took an imaging-based approach to investigate whether RNase L activity affects the
211 abundance or localization of transcriptional machinery. Pol I resides in the fibrillar
212 component of nucleoli, which is surrounded by the nucleophosmin (NPM1)-containing
213 granular component. Using antibodies against the large POLR1A subunit of Pol I and NPM1,
214 we confirmed that POLR1A formed large aggregates surrounded by a ring-like pattern of
215 NPM1 in mock-treated WT and RLKO cells (Figure 4A, Video S1-2). While the overall
216 abundance of POLR1A and NPM1 did not significantly change upon Poly(I:C) treatment
217 (Figure S4A-B), POLR1A aggregates and NPM1 rings became more dispersed in many of the
218 WT cells, but less so in the RLKO cells (Figure 4A, yellow arrow denotes a WT cell
219 exemplifying this phenotype, Video S3-4). We quantified this dispersion by calculating the

220 coefficient of variation (defined as CV=σ/μ, where σ is the standard deviation and μ is the
221 mean intensity) of POLR1A and NPM1 signals in the nucleus, with a lower CV indicating a
222 more even (i.e., dispersed) distribution of signals. This confirmed a significantly reduced
223 mean CV for both POLR1A and NPM1 in poly(I:C)-treated WT cells compared to RLKO cells
224 (Figure 4B-C). Thus, consistent with the reduced Pol I-mediated rRNA transcription observed
225 by 4sU-seq, RNase L activation leads to nucleolar disruption.

226 We next monitored the large RPB1 subunit of Pol II, which undergoes progressive
227 phosphorylation within the heptad repeats in its C-terminal domain (CTD). We used
228 antibodies recognizing either the RPB1 N-terminus (NTD, all phosphorylation states), the
229 CTD serine 5 phosphorylated (S5P) version associated with transcription initiation, and the
230 CTD serine 2 phosphorylated (S2P) version associated with elongation. Poly(I:C) treatment
231 caused a modest but significant decrease in the abundance of total (NTD) and S5P Pol II in
232 WT but not RLKO cells (Figure 4D-E, Figure S4C). We further validated the reduction of S5P
233 Pol II by using an independent antibody (3E8) (Figure S4D). We did not observe consistent
234 changes to total or phosphorylated Pol II localization, or to the abundance of S2P Pol II upon
235 poly(I:C) treatment (Figure 4F).

236 Finally, we analyzed nuclear speckles, which are hubs for Pol II co-transcriptional RNA
237 processing and undergo morphological changes in transcriptionally inhibited cells [37].
238 Although nuclear speckle size was unchanged (Figure S4E), there was an increase in SC35
239 intensity and coefficient of variation in speckles in poly(I:C)-treated WT but not RLKO cells
240 (Figure 4G-I, Figure S4F) as well as a more rounded speckle morphology (Figure S4G). Thus,
241 RNase L activation is associated with a modest reduction in the abundance of
242 unphosphorylated and S5P Pol II, as well as morphological changes to nuclear speckles and
243 nucleoli.

244

245 **RNase L represses transcription via reduction of Pol II occupancy in the gene body**

246 To directly measure how RNase L activation influences Pol II occupancy genome-wide, we
247 performed CUT&RUN-sequencing using antibodies to the Pol II S5P CTD (4H8) and Pol II S2P
248 CTD (E1Z3G) and applied yeast spike-in DNA normalization to account for potential global
249 changes in occupancy. S5P and S2P Pol II occupancy were not globally changed at the
250 transcription start site (TSS) in poly(I:C)-treated WT compared to RLKO cells or untreated
251 cells (Figure 5A-B). Analyzing subnucleosomal fragments (<120bp) and nucleosomal
252 fragments (>120bp) separately yielded similar results (Figure S5A-B), as did a differential
253 binding analysis using DiffBind to measure Pol II occupancy on a gene-by-gene basis (Figure
254 5C-D).

255 In contrast to the TSS occupancy data, when we zoomed in on the gene body and
256 transcription end site (TES) regions, we observed a reduction in S2P Pol II occupancy (Figure
257 6A). To quantify this reduction, we first calculated an elongation index, defined as the density
258 of reads in the gene body (+250bp from TSS to TES) divided by the density of reads at the TSS
259 (-500bp to +250bp from TSS) (Figure 6B), with a lower elongation index suggestive of a defect
260 of S2P Pol II traveling into the gene body. We observed an overall reduced elongation index
261 in poly(I:C)-treated WT cells compared to poly(I:C)-treated RLKO cells or mock-treated cells
262 (Figure 6C, S6A-B). This observation was further supported by a differential binding analysis
263 across windows spanning different gene regions, which showed a progressive reduction of
264 S2P Pol II binding midway through the gene body to the TES (Figure 6D-E). Approximately 30%
265 of expressed genes show reduced S2P Pol II binding at the late-elongation window and the
266 TES window (Figure 6F-G), and these also have a more pronounced reduction in 4sU RNA
267 level (Figure S6C-D). Example traces are shown in Figure 6H, demonstrating reduced S2P
268 occupancy within the gene body but no reduced S2P or S5P occupancy at the TSS of poly(I:C)
269 treated WT relative to RLKO cells. While it is possible that the loss of S2P Pol II signal is due
270 to reduced phosphorylation or enhanced dephosphorylation, such reduced S2P mark is also
271 indicative of affected Pol II elongation, given the pivotal roles of S2P mark in regulating Pol II
272 elongation [38-40]. Thus, RNase L activation negatively impacts Pol II transcription primarily
273 during the elongation phase.

274

275 **Importin β-mediated nuclear import links cytoplasmic RNA decay to transcription**

276 Finally, we sought to determine the nature of the signal linking RNase L-induced cytoplasmic
277 RNA decay with transcriptional repression in the nucleus. Accelerated cytoplasmic RNA
278 decay is known to cause differential trafficking of RNA-binding proteins from the cytoplasm
279 to the nucleus [7,20]. To determine whether protein nuclear import plays a role in
280 transcriptional repression by RNase L, we treated cells with Ibetazol, a specific inhibitor of
281 importin β-mediated nuclear import [41], prior to measuring EU incorporation in our pulse
282 labeling assay. Indeed, Ibetazol caused a significant increase in EU incorporation in
283 poly(I:C)-treated WT cells but did not alter EU incorporation in RLKO cells (Figure 7A).
284 Importantly, RNase L retained its mRNA degradation activity in Ibetazol-treated cells, as
285 measured by RT-qPCR for RPLP0 and CHMP2A (Figure 7B). Thus, nuclear import of proteins,
286 potentially those released during cytoplasmic RNA decay by RNase L, is required to induce
287 subsequent transcriptional repression.

288

289 # Discussion

290 RNase L-induced cytoplasmic mRNA degradation extensively remodels the cellular gene
291 expression landscape, influencing how cells respond to viral infection. Though originally
292 thought to mainly inhibit translation, it is now appreciated that RNase L triggers cascading
293 impacts on upstream stages of gene expression, including mRNA processing and export [6,7].
294 Here, we demonstrate through EU pulse labeling, nascent mRNA sequencing, and Pol II
295 occupancy experiments that cytoplasmic RNase L activity also profoundly impacts RNA
296 synthesis by repressing transcription, including at immune genes. RNase L-induced
297 transcriptional repression coincides with nucleolar disruption, as well as changes in nuclear
298 speckle morphology, similar to those previously reported in transcriptionally inhibited cells
299 [37]. Decay-to-transcription signaling involves protein shuttling between the two
300 compartments, as inhibition of importin β breaks this connection and restores RNA
301 synthesis (Figure 7C). The combination of these disruptions to the whole cellular gene

302 expression pathway, spanning RNA synthesis through translation and decay, is likely what
303 renders RNase L such a potent modulator of gene regulation.

304 We hypothesize that RNase L affects nascent mRNA primarily by impairing transcription
305 elongation, as the most prominent Pol II phenotype was reduced S2P Pol II occupancy at the
306 3' end of genes. However, it is possible that other stages of RNA biogenesis may also be
307 impacted, especially given our imaging data showing a modest reduction in Pol II levels
308 within the nucleoplasm. The fact that we observed reduced S5P Pol II levels by
309 immunofluorescence but not by CUT&RUN suggests that a proportion of free or unstably
310 bound S5P Pol II may undergo degradation. This could, for example, be mediated by the
311 ARMC5 E3 ligase if the Pol II is defective [42-44]. It is possible that, over time, a gradual reduction
312 in total Pol II could lead to additional effects at earlier stages of transcription, or that reduced
313 S5P Pol II selectively rather than globally impacts early-stage transcription in RNase L-
314 activated cells.

315 Our observation that RNase L activation leads to changes to Pol I, NPM1, and SC35
316 distribution is consistent with previous reports that inhibition of Pol I and Pol II transcription
317 can cause morphological changes to their respective transcription and processing sites [45-47].
318 Notably, the dispersion of Pol I and NPM1 was similarly reported in cells treated with the
319 cyclin-dependent kinase (CDK) inhibitor flavopiridol, and potentially due to inhibition of the
320 phosphorylation of Pol I co-activator Treacle [45]. Nuclear speckle-associated proteins play
321 roles in co-transcriptional RNA processing. Similar to Pol II inhibition by chemical treatment,
322 RNase L activation also altered nuclear speckle morphology, suggesting a link between
323 transcription repression to other co-transcriptional defects, including intron retention [7] and
324 reduced export [6,46] in RNase L-activated cells.

325 The fact that RNase L promotes transcriptional repression from the cytoplasm indicates that
326 its mechanism of action is indirect and requires one or more signals to be conveyed between
327 the compartments. We hypothesize this involves the relocalization of RNA-binding proteins
328 (RBPs) from the cytoplasm to the nucleus, given that blocking protein nuclear import
329 significantly increases RNA synthesis in RNase L-activated cells. More than 20 RBPs shuttle

330 into the nucleus upon their release from mRNA undergoing degradation by herpesviral
331 nucleases [20], and several similarly relocalize in RNase L-activated cells [7]. Nuclear
332 accumulation of these RBPs alters co-transcriptional RNA processing, including promoting
333 mRNA hyperadenylation and nuclear poly(A) RNA accumulation [6,7,15,48]. It is also associated
334 with transcriptional repression by herpesviral nucleases [19-21]. Thus, one possibility is that the
335 accumulation of these RBPs in the nucleus disrupts co-transcriptional processing or the
336 function of transcriptional regulators, leading to the observed elongation defects.

337 Other signals, in addition to protein redistribution, could also contribute to transcriptional
338 repression by RNase L. For example, it could be propagated by stress signals conveyed by
339 the global disruption of protein translation, e.g., as a consequence of ZAKα-dependent
340 ribotoxic stress responses or other ribosome quality control pathways induced by RNase L
341 [8,11]. In support of this hypothesis, nascent protein ubiquitinylation in response to disrupted
342 translation during heat shock contributes to transcriptional repression via a mechanism
343 involving p38 signaling [49]. Additionally, RNase L-induced translation arrest could result in a
344 loss of proteins involved in global transcription regulation, particularly those with shorter
345 half-lives. Consistent with this possibility, translation inhibition by cycloheximide in mouse
346 embryonic stem cells can lead to depletion of euchromatin modifiers like Chd1 and reduced
347 euchromatin marks, reduced Pol II occupancy, and less nascent RNA [50]. However, our
348 observation that nascent RNA synthesis was reduced as early as 2 hours post poly(I:C)
349 transfection indicates that only highly labile proteins should be affected. Finally, it is
350 possible that RNA fragments generated by RNase L cleavage serve as signaling molecules in
351 the cytoplasm or upon transit into the nucleus [51].

352 A key outcome of transcriptional repression is the modulation of immune gene transcription.
353 We find that although ISGs are robustly induced by poly(I:C) transfection independently of
354 RNase L, RNase L activity tempers their induction. Many ISGs are downregulated due to
355 reduced IFN signal amplification, which is relevant considering that RNase L activation is not
356 uniform in cultures of cells exposed to dsRNA, and thus decreased gene expression by
357 RNase L should influence innate immune signaling in neighboring cells [4,6,52]. However, there

358 are immune genes, such as IL1A, whose transcription is directly repressed by cytoplasmic
359 RNA decay, indicating that RNase L-induced transcriptional repression can have both cell-
360 autonomous and paracrine effects. Given the clinical implications of OAS and RNase L
361 mutations in autoimmune diseases, including MIS-C [1,9], elucidating how the RNA decay-
362 driven transcription repression shapes the immune landscape — in coordination with other
363 branches of RNase L-driven pathways — should remain a focus of future studies.

364

365 Limitations of the study

366 While our data support a defect in Pol II elongation in response to RNase L activation, we
367 cannot rule out additional possible defects in other stages of transcription, including
368 changes in CTD phosphorylation, initiation and pause release. We also do not know whether
369 the transcriptional defects observed for Pol I and Pol III occur via a similar or distinct
370 mechanism from that observed for Pol II. Finally, while we hypothesize that RBPs that are
371 released from degraded RNA in the cytoplasm mediate the decay-to-transcription signaling
372 during RNase L activation, an important future goal is to determine which specific proteins
373 are required for transcriptional repression.

374

375 Resource availability

376 Lead contact

377 Further information and requests for resources and reagents should be directed to and will
378 be fulfilled by the Lead Contact, Britt Glaunsinger (glaunsinger@berkeley.edu).

379

380 Materials availability

Plasmids generated in this study have been deposited to Addgene (see Key resources table for accession numbers).

DATA AND SOFTWARE AVAILABILITY

4sU-seq, S5P Pol II CUT&RUN-seq, and S2P Pol II CUT&RUN-seq datasets were deposited in NCBI Gene Expression Omnibus under the accession numbers GSE298174, GSE298175, and GSE313712, respectively. No original code was reported. Further information required for reanalysis of data reported here will be available upon request.

Acknowledgements

We thank all members of the Glaunsinger and Coscoy labs for helpful discussions. We thank James Burke and Roy Parker (CU Boulder) for providing the A549 RNase L KO and complementation cell lines and Susan Carpenter (UC Santa Cruz) for providing the iBMDM cell line. We thank Nharae Eugene Lee for generating the viral stocks used in this study. We thank Alejandro Rivera-Madera for generating the pLJM1-Halo-NLS plasmid used in this study. Imaging was performed at CRL Molecular Imaging Center (RRID:SCR_017852) and the Biological Imaging Facility at UC Berkeley, with special thanks to Holly Aaron and Denise Schichnes for training and technical support. Sequencing of the 4sU-seq samples were performed at Vincent J. Coates Genomics Sequencing Laboratory at UC Berkeley (QB3 Genomics, UC Berkeley, Berkeley, CA, RRID:SCR_022170). Sequencing of the CUT&RUN samples were performed at DNA Technologies and Expression Analysis Core at the UC Davis Genome Center, supported by NIH Shared Instrumentation Grant 1S10OD010786-01. B.G. is an investigator of the Howard Hughes Medical institute and this research was also supported by NIH R01CA136367. Diagrams were created with BioRender.

407 ## Declaration of interests

408 The authors declare no competing interests.

409

410 ## Figure legends

411 **Figure 1. RNase L-mediated mRNA degradation represses nascent RNA accumulation.**

412 (A) Diagram showing the experimental setup for nascent RNA measurement. (B) Flow
413 cytometry histograms of A549 WT or RNase L knockout (RLKO) cells with the indicated
414 treatment from one representative biological replicate (of 3 independent biological
415 replicates). (C) Quantification of flow cytometry data from 3 independent biological
416 replicates. Each dot represents the median fluorescence intensity of the sample with the
417 indicated treatment from one biological replicate, normalized to the median fluorescence
418 intensity of mock-transfected RLKO cells. Bars represent mean ± SD. P-values were
419 calculated using a two-sided Welch's *t*-test. (D) Representative immunofluorescence
420 images (max intensity projection, 3 independent biological replicates) of A549 WT or RLKO
421 cells infected with Zika virus (MOI=5) at 24 hpi. Cells were stained with mouse anti-NS3
422 antibody to indicate infected cells, and Hoechst 33342 to mark nuclei. (E) Quantification of
423 nuclear EU signal in 1 representative replicate of 3 independent biological replicates in *(D)*.
424 Each dot represents the mean nuclear EU fluorescence intensity of one individual nucleus.
425 Bars represent mean ± SD. P-value was calculated using Welch's *t* test.

426 **Figure 2. RNase L reduces nascent rRNA and pre-mRNA.**

427 (A) Diagram summarizing the 4sU-seq experiment. (B) IGV tracks showing 4sU-seq coverage
428 at rDNA repeat. Tracks represent the average coverage of 3 independent biological replicates.
429 Coverage depth is shown in brackets in the upper track, with a positive value indicating
430 coverage in the positive strand direction, and a negative value indicating coverage in the
431 negative strand direction. (C) Metagene analysis of 4sU-seq signal coverage over expressed
432 protein-coding genes (-1kb from TSS to +2.5kb from TES, n=12,713). Lines represent the
433 average coverage of 3 independent biological replicates. (D) Differential expression analysis
434 of 4sU-seq comparing WT cells transfected with poly(I:C) to RLKO cells transfected with
435 poly(I:C). Each gene was plotted with the log2(fold change) value on the y-axis and the log2
436 of the mean expression level, expressed in counts per million (CPM), on the x-axis.
437 Significantly-up (red) and significantly-down (blue) are defined as adjusted *p*-value < 0.05
438 and log2(fold change) > 0.585 or <-0.585, respectively. Dashed lines denote log2(fold change)
439 of -0.585, 0, and 0.585. (E) GO-term enrichment analysis of down-regulated genes identified
440 in *(D)*. (F) IGV tracks showing 4sU-seq signal coverage on RPL13, an example of ribosomal
441 protein genes, and RSAD2, an example of immune genes. Coverage depth is shown in
442 brackets in the upper track, with a positive value indicating coverage in the positive strand
443 direction, and a negative value indicating coverage in the negative strand direction. (G) Pre-
444 mRNA level of immune genes in WT or RLKO cells transfected with poly(I:C), with or without
445 treatment of brefeldin A (BFA). Pre-mRNA level is determined by RT-qPCR using intron-exon
446 spanning primer pairs, normalized to 18S. *, p< 0.05; **, p<0.01; ***, p< 0.001; ns, not
447 significant.

448 **Figure 3. Reduction of nascent RNA is not due to accelerated nuclear RNA degradation**
449 **by RNase L.**

450 (A) Quantification of EU signal intensity after uridine chase for durations indicated. Each
451 point represents the average of median EU fluorescence intensity from 3 independent
452 biological replicates, normalized to 0h chase. (B) Diagrams of the constructs used. (C)
453 Representative images of the localization of tagged RNase L. The tagged RNase L was
454 visualized by halo tag labeling with JF646 halo dye. A single z plane is shown per construct.
455 (D) Line profile of CRS-Halo-RNase L shown in *(C)*. (E) Line profile of Halo-RNase L shown in
456 *(C)*. (F) Flow cytometry scatter plot of A549 RLKO cells nucleofected with the indicated
457 constructs, with or without poly(I:C) transfection. Data is from 1 representative replicate of
458 3 independent biological replicates. (G-I) Quantification of EU signals in *(F)*. The Halo
459 intensity is gated at locations shown in (F) and separated into 2 populations. Each dot
460 represents the median fluorescence intensity, normalized to the median fluorescence
461 intensity of mock-transfected RLKO cells nucleofected with the constructs indicated. Bars
462 represent mean ± SD. P-values were calculated using a ratio paired *t*-test.

Figure 4. RNase L disperses nucleoli and reduces serine-5-phosphorylated Pol II levels in the nucleus.

(A) Max-intensity-z-projection images showing POLR1A and NPM1 localization in poly(I:C)-transfected A549 WT or RLKO cells. Yellow arrows point to examples of nuclei showing the dispersal phenotype. (B-C) Quantification of the coefficient of variation (CV) of POLR1A (*B*) or NPM1 (*C*) in the nucleus, defined as $CV=\sigma/\mu$, where σ is the standard deviation, and μ is the mean intensity. (D-F) Quantification of mean Pol II (NTD) (*D*), S5P (*E*), and S2P (*F*) staining intensity in poly(I:C)-transfected A549 WT or RLKO cells. (G) Max-intensity-z-projection images of SC35 localization in poly(I:C)-transfected A549 WT or RLKO cells. (H-I) Quantification of mean SC35 intensity for each SC35 focus (*H*) and the coefficient of variation of SC35 in the nucleus (*I*), using data in *(D)*. In all graphs, each point represents the value calculated for each nucleus. Error bars represent mean ± SD. ****, $p<0.0001$ (Welch's t-test). The imaging data shown is representative of 3 independent biological replicates.

Figure 5. RNase L activation does not broadly inhibit Pol II occupancy at transcription start sites.

(A-B) Metagene analysis of S5P (*A*) and S2P (*B*) Pol II occupancy at -1kb to +1kb around transcription start site (TSS) on expressed protein-coding genes in WT or RLKO cells, either mock-transfected or transfected with poly(I:C). Lines represent the average coverage of 3 independent biological replicates. (C-D) Differential binding analysis of S5P (*C*) and S2P (*D*) Pol II CUT&RUN-seq signal at the TSS (-500bp to +250bp) comparing WT cells transfected with poly(I:C) to RLKO cells transfected with poly(I:C). Significantly-up (red) and significantly-down (blue) are defined as adjusted *p*-value < 0.05 and log2(fold change) > 0.585 or < -0.585, respectively. Dashed lines denote log2(fold change) of -0.585, 0, and 0.585.

Figure 6. RNase L activation reduces S2P RNA Pol II occupancy in the gene body.

(A) Metagene analysis of S2P Pol II occupancy on expressed protein-coding genes in WT or RLKO cells, either mock-transfected or transfected with poly(I:C). The lower panel represents a zoom-in view of coverage from the TSS to 2Kb after TES. Lines represent the average coverage of 3 independent biological replicates. (B) Diagram depicting the calculation of the elongation index and the range of the TSS window and the gene-body window. (C) Scatterplot showing the changes in the elongation index in relation to the read density in the gene body. The median and interquartile range of the changes in elongation index are shown to the right. ****, $p < 0.0001$ using one-sample t-test, comparing to 0. (D) Diagram depicting the range of promoter (Prom), early-elongation (early), mid-elongation (mid), late-elongation (late), and TES windows. (E) Summary of log2 fold changes comparing WT to RLKO cells, both transfected with poly(I:C), at windows defined in (*D*). Each dot represents the log2 fold change of S2P binding at the corresponding window within a gene, calculated by diffBind. Only genes longer than 3.2kb were included to minimize overlap. Number n represents quantifiable loci retained by diffBind after filtering. Error bars represent the median and interquartile range. (F-G) Zoom in view of the differential binding analysis in (*E*) of S2P Pol II CUT&RUN signal at the late elongation windows (-1100 bp to -100 bp from TES) (*F*) or TES windows (-50 bp to +950 bp from TES) (*G*). Significantly-up (red) and significantly-down (blue) are defined as adjusted *p*-value < 0.05 and log2(fold change) > 0.585 or < -0.585, respectively. Dashed lines denote log2(fold change) of -0.585, 0, and 0.585. (H) IGV tracks showing Pol II 4sU-seq, S2P CUT&RUN, and S5P CUT&RUN signal coverage on the housekeeping genes SLC7A11 and HSP90AA1 and the immune gene IL1A. All tracks represent the average coverage of 3 independent biological replicates. Coverage depth is shown in brackets in the upper track. For 4sU-seq tracks, a positive value indicating coverage in the positive strand direction, and a negative value indicating coverage in the negative strand direction.

Figure 7. Inhibition of importin-β dampens transcription repression by RNase L

(A) Quantification of nuclear EU signal in WT or RLKO cells with indicated treatments. The data represent one representative replicate of four independent biological replicates. Each dot represents the mean nuclear EU fluorescence intensity of one individual nucleus. Bars represent mean ± SD. P-value was calculated using Welch's *t* test. (B) RT-qPCR measuring the indicated housekeeping mRNA after poly(I:C) transfection in WT or RLKO cells, with or without ibetazol. Ns, not significant ($p > 0.05$ calculated with two-sided Welch's *t* test). (C) Diagram depicting a model of RNase L-dependent transcription repression.

526 **Figure S1. RNase L activation reduces nascent RNA progressively in A549 and iBMDM**
527 **cells, independent of caspase activity. Related to Figure 1.**

528 (A) Representative max-intensity-projected images of mock-transfected A549 WT cells
529 pulsed with 1mM EU for 30 minutes. (B) Normalized fluorescence intensity across line trace
530 in (*A*). (C) A549 WT or RLKO cells were either mock-transfected with RNAiMAX or transfected
531 with 0.76μg/ml poly(I:C) for durations indicated, followed by a 30-min pulse labeling with 1
532 mM EU. Error bars represent the mean ± SD of log2-fold change over mock-transfected
533 RNase L KO cells at the indicated time point. Data is from 2 biological replicates. (D)
534 Quantification of nuclear EU signal in WT or RLKO cells, either mock-transfected or
535 transfected with synthetic 2-5A. The data show one representative replicate of two
536 independent biological replicates. Each dot represents the mean nuclear EU fluorescence
537 intensity of one individual nucleus. Bars represent mean ± SD. ****, $p < 0.0001$; P-value was
538 calculated using two-sided Welch's *t* test. (E) Quantification of the percentage of EU low
539 cells. Error bars represent mean ± SD of 3 biological replicates. P-value was calculated using
540 two-sided Welch's *t* test. (F) A representative flow cytometry histogram of murine iBMDM
541 cells with treatments indicated. EU signal was gated according to no-EU controls, shown
542 with a dashed line. (G) Western blot validation of RNase L siRNA knockdown efficiency.
543 Numbers below lanes indicate relative levels of bands normalized to the control KD of the
544 corresponding replicate. (H) A549 WT or RNase L KO cells were transfected with 0.76μg/ml
545 poly(I:C) in the presence of z-VAD at the indicated concentration for 4 hours, followed by 30-
546 min pulse labeling with 1mM EU. Each dot represents the median fluorescence intensity of
547 the sample with indicated treatment from one biological replicate, normalized to the median
548 fluorescence intensity of DMSO-treated KO cells. Bars represent mean ± SD. (I) Low
549 magnification (20X) field of view of Zika virus-infected cells, from the same sample as *Figure*
550 *1D-E*.

551 **Figure S2. 4sU-seq data accurately captures changes on the nascent RNA level. Related**
552 **to Figure 2.**

553 (A) Differential expression analysis of 4sU-seq comparing WT cells to RLKO cells transfected
554 with poly(I:C) cells (same as Figure 2D), with spike-ins highlighted. See Figure 2D for details.
555 (B) RT-qPCR of 4sU samples compared to no-4sU control. RNA samples were the same as
556 the ones used in 4sU-seq. *, $p < 0.05$ (ratio paired *t* test). (C) IGV tracks showing 4sU-seq
557 signal coverage on RN7SK, VTRNA1-3 and RN7SL3, examples of downregulated Pol III
558 transcribed genes. Tracks represent the average coverage of 3 independent biological
559 replicates. In this and subsequent tracks, a positive value indicates coverage in the positive
560 strand direction, while a negative value indicates coverage in the negative strand direction,
561 and coverage depth is shown in brackets in the upper track. (D) Differential expression
562 analysis of 4sU-seq comparing mock-transfected WT cells RLKO cells. (E) IGV tracks
563 showing 4sU-seq signal coverage on CADM2, an example of cell line-specific expression
564 variation. Tracks represent the average coverage of 3 independent biological replicates. (F)
565 IGV tracks showing 4sU-seq signal coverage on FAP downstream of IFIH1, an example of
566 read-through transcription. Tracks represent the average coverage of 3 independent
567 biological replicates. (G) Pre-mRNA level of additional immune genes in WT or RLKO cells
568 transfected with poly(I:C), with or without treatment of brefeldin A (BFA). Pre-mRNA level is
569 determined by RT-qPCR using intron-exon spanning primer pairs, normalized to 18S. *, $p<$
570 0.05; **, $p<0.01$; ***, $p< 0.001$; ns, not significant; calculated with two-sided Welch's *t* test.

571 **Figure S3. EU pulse chase experiments accurately measure nuclear RNA turnover**
572 **kinetics and functional confirmation of the CRS tag. Related to Figure 3.**

573 (A) Diagram showing the experimental setup of the "EU pulse last" control in parallel to the
574 EU pulse chase experiments shown in Figure 3A. (B) Quantification of EU signal in the "EU
575 pulse at last" control. Data from Figure 3B, replotted as the ratio of EU signals in A549 WT to
576 RLKO cells, are included for comparison. Each dot represents one biological replicate. Bars
577 represent mean ± SD. (C) Representative max-intensity-projected images of cells
578 transfected with poly(I:C) for 1 hour, pulsed with 1mM EU for 30 minutes then chased for 2
579 hours. WT cells were labeled with CFDA-SE dye and co-cultured with RLKO cells. (D)
580 Normalized fluorescence intensity across line trace in *(C)*. CFDA-SE signal is included as a
581 uniform distributed control for comparison. (E) Representative images of the localization of
582 CRS-Halo-NLS and Halo-NLS. A single z plane is shown per construct. Diagram showing the
583 constructs are included.

584 **Figure S4. RNase L activation reduces total and S5P Rpb1 levels in the nucleus and does**
585 **not affect nuclear speckle size. Related to Figure 4.**

586 (A-B) Quantification of mean POLR1A (A) and NPM1 (B) staining intensity in poly(I:C)-
587 transfected A549 WT or RLKO cells. (C) Representative max-intensity-z-projection images of
588 Pol II (NTD), S5P, and S2P staining in A549 WT or RLKO cells transfected as indicated. Data
589 are the same as Figure 4D-F. (D) Quantification of mean S5P-RPB1 staining intensity using
590 3E8 antibody in poly(I:C)-transfected A549 WT or RLKO cells. Each point represents the
591 mean intensity calculated for each nucleus. Error bars represent mean ± SD. ****, $p<0.0001$
592 (Welch's t-test). Data represents 1 replicate of 2 independent biological replicates. (E)
593 Quantification of SC35 foci area for each SC35 focus using data in Figure 4D. Each point
594 represents the value measured for each SC35 focus. Error bars represent mean ± SD. Data
595 are from 1 representative replicate of 3 total replicates. (F) Max-intensity-z-projection images
596 of SC35 localization in mock or poly(I:C)-transfected A549 WT or RLKO cells. Data from
597 Figure 4G is included for comparison. (G) Quantification of mean SC35 circularity for each
598 SC35 focus using data in Figure 4*G* and Figure S4F. Each point represents the value
599 calculated for each SC35 focus. Error bars represent mean ± SD. ****, $p<0.0001$ (two-sided
600 Welch's t-test).

601
602

603

604

605 **Figure S5. RNase L activation does not reduce CUT&RUN subnucleosomal and**
606 **nucleosomal signals at TSS. Related to Figure 5.**

607 (A) Metagene analysis of S5P and S2P Pol II CUT&RUN subnucleosomal fragment (<120bp)
608 coverage at -1kb to +1.5kb around transcription start site (TSS) of expressed protein-coding
609 genes. (B) Metagene analysis of S5P and S2P Pol II CUT&RUN nucleosomal fragment
610 (>120bp) coverage at -1kb to +1.5kb around the transcription start site (TSS) of expressed
611 protein-coding genes. The enrichment of subnucleosomal fragments slightly upstream of
612 TSS and the bimodal peaks around the TSS of the nucleosomal fragments likely reflect the
613 local nucleosome organization around Pol II occupancy sites.

614

615 **Figure S6. RNase L activation reduces S2P Pol II CUT&RUN signal in the gene body,**
616 **which correlates with the reduction in 4sU-seq signal. Related to Figure 6.**

617 (A) Empirical cumulative distribution function (ECDF) plot of log2(elongation factor) for WT
618 or RLKO cells, either mock-transfected or transfected with poly(I:C). P values were
619 calculated with two-sided Kolmogorov–Smirnov tests. (B) Scatterplot showing the changes
620 in elongation index between poly(I:C)-transfected WT cells and mock-transfected WT cells
621 in relation to the read density in the gene body. (C-D) Scatterplot showing the relation
622 between log2 fold change of 4sU-seq and S2P Pol II occupancy at late (*C*) or TES windows
623 (*D*). Up- or down-regulated S2P is defined in the same way as Figure 6F-G.

624

625 # STAR METHODS

626 **Key resources table**

REAGENT or RESOURCE	SOURCE	IDENTIFIER
Antibodies		
mouse anti-NS3 antibody (Clone E1D8)	Balsitis et al., 2009[53]	N/A
POLR1A (D6S6S) Rabbit mAb	Cell Signaling Technology	Cat# 24799; RRID:AB_2798884
Nucleophosmin antibody [FC82291]	Abcam	Cat# ab10530; RRID:AB_297271
Rpb1 NTD (D8L4Y)	Cell Signaling Technology	Cat# 14958; RRID:AB_2687876
Rpb1 S5P CTD (ab5131) (for immunofluorescence)	Abcam	Cat# ab5131, RRID:AB_449369
Rpb1 S5P CTD (3E8) (for immunofluorescence)	Active Motif	Cat# 61085, RRID:AB_2687451
Rpb1 S5P CTD (4H8) (for CUT&RUN)	Cell Signaling Technology	Cat# 2629, RRID:AB_2167468
Rpb1 S2P CTD (E1Z3G) (for CUT&RUN)	Cell Signaling Technology	Cat# 13499, RRID:AB_2798238
Rpb1 S2P CTD (ab5095) (for immunofluorescence)	Abcam	Cat# ab5095, RRID:AB_304749
Mouse Anti-SC35 Monoclonal Antibody	Abcam	Cat# ab11826, RRID:AB_298608
Recombinant Anti-RNase L antibody [EPR15894]	Abcam	Cat# ab191392, RRID:AB_2916269
GAPDH antibody [6C5]	Abcam	Cat# ab8245, RRID:AB_2107448
goat anti-rabbit IgG AlexaFluor Plus 488	Thermo Fisher Scientific	Cat# A32723, RRID:AB_2633275
goat anti-mouse IgG AlexaFluor 546	Thermo Fisher Scientific	Cat# A-11035, RRID:AB_2534093
donkey anti-rat IgG AlexaFluor Plus 488	Thermo Fisher Scientific	Cat# A48269, RRID:AB_2893137
goat anti-rabbit IgG AlexaFluor 647	Thermo Fisher Scientific	Cat# A27040, RRID:AB_2536101
Goat Anti-Rabbit IgG-HRP	SouthernBiotech	Cat# 4030-05, RRID:AB_2687483
Mouse normal IgG	Santa Cruz Biotechnology	Cat# sc-2025, RRID:AB_737182
Bacterial and virus strains		
Zika virus (Nica 2–16)	Tabata et al., 2016[54]	GenBank accession KX421194.1
Chemicals, peptides, and recombinant proteins		
4-thiouridine (4SU)	Sigma Aldrich	T4509-100MG
HPDP-Biotin	Thermo Fisher Scientific	PI21341
pAG-MNase	Cell Signaling	40366S
proteinase K	Cell Signaling	10012S

RNase A	Thermo Fisher Scientific	EN0531
4-Thio-UTP	Jena Bioscience	NU-1156S
T7 RNA polymerase	NEB	M0251L (25,000U)
CFDA-SE	Cayman Chemical	14456
5-Ethynyl-uridine	Lumiprobe	2439-500mg
Sulfo-Cyanine5-Azide	Lumiprobe	A3330
Alexa Fluor 488 Azide	Thermo Fisher Scientific	A10266
Ibetazol	Axon MedChem	Axon 4300
In-Fusion® snap assembly (master mix)	Clontech (TaKaRa)	638943
TURBO DNase	Thermo Fisher Scientific	AM2239 (5,000U)
AMV Reverse Transcriptase	Promega	M5101 (300U)
cOmplete EDTA-free protease inhibitor cocktail	Roche	5056489001
Halt Protease and Phosphatase Inhibitor Cocktail (100X)	Thermo Fisher Scientific	78440
Poly(I:C) (HMW)	InVivoGen	tlrl-pic
Lipofectamine RNAiMAX	Thermo Fisher Scientific	13778150
Brefeldin A Solution (1000X)	Thermo Fisher Scientific	00-4506-51
Janelia Fluor 646 HaloTag Ligand	Promega	GA1121
Critical commercial assays		
KAPA Stranded RNA-Seq Kit with RiboErase (HMR)	Roche	KK8484 07962304001
KAPA Single-Indexed Adapter Kit	Roche	KK8700 08005699001
ERCC RNA Spike-In Mix	Thermo Fisher Scientific	4456740
NEBNext Ultra II DNA Library Prep Kit	NEB	cat # E7645L
NEBNext Multiplex Oligos for Illumina (Unique Dual Index UMI Adaptors DNA Set 1)	NEB	cat # E7395S
Universal Mycoplasma Detection Kit	ATCC	50189644FP
iTaq universal SYBR green supermix	Bio-Rad	1725121
Q5 Hot Start High-Fidelity 2X Master Mix	NEB	M0494S
Deposited data		
Raw and processed 4sU-seq data	This study	GEO: GSE298174
Raw and processed CUT&RUN-seq data	This study	GEO: GSE298175
Total RNA-seq for mock- or poly(I:C)-transfected A549 cells	Burke et al., 2019[2]	GEO: GSE124144
Experimental models: Cell lines		
A549 WT cells	Burke et al., 2019[2]	N/A
A549 RLKO cells	Burke et al., 2019[2]	N/A
A549 RLKO cells reconstituted with 3xflag-RNase L (A549 RLKO-RL)	Burke et al., 2019[2]	N/A

A549 RLKO cells reconstituted with catalytic dead 3xflag-RNase L (R667A) (A549 RLKO-CM)	Burke et al., 2019[2]	N/A
Murine immortal bone-marrow-derived macrophages (iBMDM)	Robinson et al., 2021[55]	N/A
Oligonucleotides		
2-5A ($pA(_{2-5}A)_4$)	IDT	N/A
ON-TARGETplus Non-targeting Control Pool	Dharmacon	D-001810-10-05
SMARTPool: ON-TARGETplus Mouse RNASEL siRNA ,10nM	Dharmacon	L-043480-00-0010
Table S1	This paper	N/A
Recombinant DNA		
pLJM1-Halo-RNaseL	This study	Addgene: 250856
pLJM1-CRS-Halo-RNaseL	This study	Addgene: 250857
pLJM1-CRS-Halo-NLS	This study	Addgene: 250859
pLJM1-Halo-NLS	This study	Addgene: 250858
Software and algorithms		
HTStream		RRID:SCR_018354
STAR	Dobin et al., 2013[56]	RRID:SCR_004463
FeatureCounts	Liao et al., 2014[57]	RRID:SCR_012919
Limma-voom	Ritchie et al., 2015[58]	RRID:SCR_010943
topGO	DOI: 10.18129/B9.bioc.topGO	RRID:SCR_014798
Deeptools	Ramirez et al., 2016[59]	RRID:SCR_016366
Trimmomatic	Bolger et al., 2014[60]	RRID:SCR_011848
Bowtie 2	Langmead and Salzberg., 2012[61]	RRID:SCR_016368
SAMTOOLS	Li et al., 2009[62]	RRID:SCR_002105
UMI-tools	Smith et al., 2017[63]	RRID:SCR_017048
DiffBind	Ross-Innes et al., 2012[64]	RRID:SCR_012918
FIJI	Schindelin et al., 2012[65]	RRID:SCR_002285
ImageJ	Schneider et al., 2012[66]	RRID:SCR_003070
Prism 10 v10.3.0	GraphPad	N/A
R	www.r-project.org	N/A
RStudio	www.rstudio.com	N/A
Other		
Dynabeads MyOne Streptavidin C1	Thermo Fisher Scientific	65002

627

628 # CONTACT FOR REAGENT AND RESOURCE SHARING

629 Further information and requests for resources and reagents should be directed to and will
630 be fulfilled by the Lead Contact, Britt Glaunsinger (glaunsinger@berkeley.edu).

631

632 Experimental model and subject details

633 A549 WT, RLKO, RLKO-RL and RLKO-CM cell lines [2] were generously provided by James
634 Burke (University of Florida Scripps) and Roy Parker (University of Colorado, Boulder).
635 Immortalized murine bone marrow macrophages [55] were generously provided by Susan
636 Carpenter (UC Santa Cruz). All cell lines were maintained in DMEM supplemented with 10%
637 FBS and tested for mycoplasma routinely using Universal Mycoplasma Detection Kit (ATCC,
638 cat # 50189644FP).

639

640 # METHOD DETAILS

641 **Plasmids**

642 All plasmids generated in this study were sequence verified by whole plasmid sequencing
643 and have been deposited on Addgene, with accession numbers indicated in the Key
644 Resources Table. All PCR reactions were performed using Q5 2X master mix (NEB, cat #
645 M0494S). Sequences encoding the CRS tag, HALO tag, and RNase L with appropriate
646 overhangs were PCR amplified. pLJM1-Halo-RNaseL was constructed by directly cloning the
647 HALO and RNase L PCR fragments into linearized pLJM1-puro [67] using InFusion (Takara Bio,
648 Cat # 639650). pLJM1-CRS-Halo-RNaseL was constructed by first assembling CRS, HALO
649 and RNase L PCR fragments into a single fragment by overlap extension PCR, followed by
650 cloning into linearized pLJM1-puro using InFusion. pLJM1-CRS-Halo-NLS was generated
651 from pLJM1-CRS-Halo-RNaseL using a site-directed mutagenesis protocol described
652 previously [68] to replace RNase L fragment with an SV40 NLS (PKKKRKV). pLJM1-Halo-NLS
653 was generated from pLJM1-Halo-RNaseL using the same mutagenesis method as above.

654

655 **EU pulse chase for flow cytometry**

656 Cells were were mock-transfected, transfected with 0.76µg/ml poly(I:C) HMW (InVivoGen,
657 cat # tlrl-pic), or 10µM 2-5A ($pA(_{2\text{-}5}A)_4$, custom synthesized by IDT) using Lipofectamine
658 RNAiMAX (Thermo Fisher, cat # 13778-150) as indicated, then the media was replaced with
659 1mM EU (Click Chemistry Tools cat #CCT-1261-500 or Lumiprobe cat # 2439-500mg) in
660 DMEM with 10% FBS. The cells were incubated at 37°C for 30 minutes. For flow cytometry
661 samples, cells were washed once with 1ml PBS, harvested, and fixed with 1% PFA. The cells
662 were then permeabilized by resuspending in 100ul 0.05% w/v saponin in PBS. To visualize EU
663 incorporation, 500ul click reaction mix (4mM $CuSO_4$, 100mM sodium ascorbate, 2 µM sulfo-
664 cyanine5-azide (Lumiprobe cat# A3330) in TBS, 50mM Tris-HCl, pH 8.0, 150mM NaCl) was
665 added to the cell suspension and the samples were incubated at room temperature for 30
666 minutes, protected from light. The samples were then washed twice with 1ml 0.05% w/v
667 saponin in PBS, once with 1ml PBS, then resuspended in PBS before flow cytometry analysis.
668 The samples were then analyzed on an BD Accuri C6 Plus flow cytometer.

669 For EU pulse chase experiments, WT cells were first color-labeled with 1 µM CFDA-SE
670 (Cayman Chemical, cat # 14456) in PBS for 10 min at room temperature, quenched with
671 equal volume of DMEM with 10% FBS, then washed with DMEM with 10% FBS 3 times. The
672 labeled WT cells were resuspended in DMEM with 10% FBS, pooled with unlabeled RLKO
673 cells at a 1:1 ratio and were seeded in 6-well plates the day before experiment. Cells were
674 transfected with 0.76µg/ml poly(I:C) HMW (InVivoGen, cat # tlrl-pic) using Lipofectamine
675 RNAiMAX (Thermo Fisher, cat # 13778-150) for 1 hour and pulsed with 1mM EU in DMEM with
676 10% FBS for 30 minutes at 37°C. The EU-containing media was removed, and cells were
677 washed with PBS once and immediately chased with 10mM uridine in DMEM with 10% FBS.
678 The samples were harvested at the indicated time-points. An additional well without
679 transfection and EU pulse labeling was harvested at the same time as the 0-hour chase
680 samples, serving as a no-EU control. The "Pulse last" sample, which served as a control for
681 transfection efficiency, was transfected with 0.76µg/ml poly(I:C) for 1 hour, incubated DMEM

682 with 10% FBS without EU for 30 minutes at 37°C, washed with PBS once and replaced the
683 supernatant with DMEM with 10% FBS and incubated for 1.5 hours. Then the cells were
684 pulsed with 1mM EU in DMEM with 10% FBS for 30 minutes at 37°C and harvested at the
685 same time as the 2-hour chase samples.

686 To characterize EU incorporation in cells overexpressing tagged RNase L, A549 RLKO cells
687 were first nucleofected with the indicated construct using Neon transfection system
688 (Invitrogen) according to the manufacturer's recommended settings for A549 cells (1230V,
689 30ms, 2 pulses), using 5µg DNA per 750,000 cells in 100µL E2 buffer. The nucleofected cells
690 were cultured in 6-well plates overnight. The cells were then incubated with 20nM Halo
691 ligand Janelia Fluor 646 (Promega, cat # GA1121) diluted in 1mL DMEM + 10%FBS per well
692 30 minutes prior to poly(I:C) transfection, then transfected with 0.76µg/ml poly(I:C) for 4
693 hours without removing the Halo dye and pulsed with 1mM EU for 30 minutes same as above.
694 The samples were processed as above, with the exception that 5uM Alexa Fluor™ 488 Azide
695 (Thermo Fisher, cat #A10266) was used.

696 To characterize EU incorporation in murine iBMDM cells depleted of RNase L, cells were
697 maintained in DMEM with 10% FBS and grown to 90% confluence. Cells were removed and
698 washed once with Dulbecco's phosphate-buffered saline (DPBS) (Gibco). Nucleofections
699 were done using the Neon Transfection System (Thermo Fisher). 2×10^6 cells were
700 resuspended in 100 µL of buffer R, to which control non-targeting or RNase L targeting pools
701 of siRNA (ON-TARGETplus SMARTpool siRNA – Horizon Discovery) were added to a final
702 concentration of 200nM. This was loaded into a Neon 100-µL pipette tip and Neon tube with
703 3 mL of buffer E2 with electroporation parameters set to 1,680 V, 20 ms, 1 pulse. Following
704 electroporation, cells were plated in 10 mL of DMEM with 10% FBS in 10 cm TC-treated
705 plates and were incubated at 37°C for 24 hours. Cells were then transfected with 0.76µg/ml
706 poly(I:C) pulsed with 1mM EU for 30 minutes same as above. The samples were processed
707 as above.

708 **Immunofluorescence**

709 For Zika infection in Figure 1D-E and Figure S1G, A549 WT or RLKO cells were seeded in glass-
710 bottomed 24 well-plates at a density of 100,000 cells per well the day before the experiment,
711 and after media change, were infected with Zika virus (Nica 2–16, GenBank accession
712 KX421194.1) at an MOI = 5 for 24 hours. Cells were treated with 1 mM EU for 30 minutes
713 before being washed once with 1 mL of PBS, then fixed with 4% PFA for 15 minutes. The cells
714 were then permeabilized with 0.5% Triton X-100 in PBS for 15 minutes and washed 3 times
715 with PBS. Samples were then incubated with 500 µL of click reaction mix at room
716 temperature for 30 minutes, followed by two washes with PBS and storage in PBS. Samples
717 were then blocked with 1% BSA in PBS with 0.02% Tween-20 for 1 hour and incubated with
718 mouse anti-NS3 antibody (Clone E1D8) diluted 1:100 in the blocking solution (Balsitis et al.,
719 2009). The samples were then washed three times with PBS + 0.02% Tween-20, incubated
720 with goat anti-mouse IgG AlexaFluor Plus 488 (Invitrogen, cat #A32723) diluted 1:1000 in
721 blocking solution, and washed three times with PBS + 0.02% Tween-20. The nuclei were
722 stained with 8 µM Hoechst 33342 in PBS for 30 minutes, followed by 2 PBS washes.

723 For RNase L localization studies, A549 RLKO cells were nucleofected as in the "EU pulse
724 chase for flow cytometry" section and 340,000 cells were seeded per well in a glass-
725 bottomed 24-well plate and incubated overnight. Cells were first labeled with 20nM Halo
726 ligand Janelia Fluor 646 for 30 minutes and transfected with poly(I:C) at a concentration of
727 0.76µg/ml for 4 hours without removing the Halo ligand. The cells were then pulse labeled
728 with EU and fixed, permeabilized, labeled with click reaction and Hoechst 33342 as above.

729 For characterizing changes in POLR1A, NPM1, RPB1 and nuclear speckle morphology, A549
730 WT or RLKO cells were seeded in glass-bottomed 24 well-plates at a density of 100,000 cells
731 per well the day before experiment and transfected with either lipofectamine RNAiMAX alone
732 or with poly(I:C) at a concentration of 0.76µg/ml for 4 (optionally pulsed with 1mM EU for
733 30min) to 4.5 hours. Samples fixed and permeabilized and optionally labeled with click
734 reaction as above, then were blocked with 0.3%-0.5% BSA in PBS with 0.3-0.5% Triton X-100
735 for 0.5-1 hour. Then samples were stained with primary antibodies against POLR1A (clone
736 D6S6S, Cell Signaling, #24799, 1:500), NPM1 (Abcam, ab10530-100, 1:500), Rpb1 NTD
737 (clone D8L4Y, Cell Signaling Technology, 1:500), Rpb1 S5P (ab5131, Abcam, 1:500; or 3E8,

738 Active Motif, RRID:AB_2687451), Rpb1 S2P (ab5095, Abcam, 1:500) and SC35 (ab11826,
739 Abcam, 1:500) diluted in blocking solution overnight at 4°C, goat anti-rabbit IgG AlexaFluor
740 Plus 488 (Invitrogen, cat #A32723) alone or goat anti-mouse IgG AlexaFluor 546 (Invitrogen,
741 cat # A11035), donkey anti-rat IgG AlexaFluor Plus 488 (Invitrogen, cat # A48269), and goat
742 anti-rabbit IgG AlexaFluor 647 (Invitrogen, cat # A27040) diluted 1:1000 in blocking solution
743 as secondaries, and 8-10μM Hoechst 33342.

744 For Ibetazol treatment, A549 WT or RLKO cells were seeded in glass-bottomed 24 plates at
745 a density of 100,000 cells per well the day before the experiment and transfected with
746 poly(I:C) at a concentration of 0.76μg/ml for 3 hours in the presence of DMSO or 50 μM
747 Ibetazol. Cells were then pulse labeled with EU and fixed, permeabilized, labeled with click
748 reaction.

749 All samples were imaged on a Nikon Eclipse Ti spinning disk confocal microscope or a Zeiss
750 LSM 880 laser scanning microscope.

751

752 **Image processing**

753 All confocal image processing was performed using FIJI [65], either manually or with custom
754 macros. Line profile measurements were performed using the plot profile function, and the
755 data were exported to Prism 10 for normalization and visualization. For nuclear signal
756 quantification in Figure 1D-E and Figure 4D-F, the nuclear regions of interest (ROIs) were
757 generated from the Hoechst channel in the image z-stack by Gaussian blur, thresholding
758 with the Otsu method, and 3D segmentation using the 3D Manager. To fill holes within ROIs
759 and exclude objects on edges, the 3D segmentation map was converted to binary, followed
760 by "3D fill holes" and "3D exclude edges". The processed binary map was 3D segmented
761 again using the 3D Manager to generate the final ROIs. The ROIs were then used to quantify
762 mean intensity in selected channels with the "quantify" function in 3D Manager.

763 For quantification in Figure 4B-C, H-I, 7A, and S4D, the image z-stack was first max-intensity
764 or sum-intensity projected. Then the nuclear ROIs were generated from the Hoechst channel

765 by Gaussian blur, thresholding with the Otsu method, hole filling by the "Fill holes" function,
766 and size selected with the "Analyze particle" function to only include particles larger than 50
767 μm^2. Then the ROIs were used to quantify mean intensity and standard deviation in selected
768 channels with the "Measure" function. For nuclear speckle analysis, a binary mask for the
769 nuclei was first generated, then the channels of interest were multiplied to the mask to
770 isolate nuclei. A duplicated SC35 channel was then used to generate nuclear speckle ROIs
771 by Gaussian blur, local thresholding with the Bernsen method, size selected with the
772 "Analyze particle" function to only include particles larger than 0.4 μm^2. Then the ROIs were
773 used to quantify mean intensity, area, and circularity in original SC35 channel with the
774 "Measure" function.

775

776 **4sU-spike-in RNA production using in-vitro transcription**

777 4sU-labeled or unlabeled spike-in RNA was produced according to a protocol described
778 previously with modifications [69]. Briefly, ERCC RNA Spike-In Mix (Thermo Fisher, 4456740)
779 was reverse transcribed using AMV-RT (Promega, cat # M5108) and random 9-mer primer
780 (IDT). Amplicons containing the T7 promoter were amplified using primers in Table S1 and
781 Q5 2X master mix. In vitro transcription was performed using T7 RNA polymerase (NEB,
782 M0251L) and 5 mM each of ATP, GTP, and CTP. For labeled spike-in, 4.5mM UTP and 0.5mM
783 4-thio-UTP (Jena Bioscience, NU-1156S) were used; for unlabeled spike-in, 5mM UTP was
784 used. Template DNA was then digested with TURBO DNase. RNA was then purified by
785 phenol:chloroform extraction and cleaned up with Zymo RNA clean and concentrator -5 to
786 remove unincorporated 4-thio-UTP. An equal mass of 3 labeled spike-in RNAs and 3
787 unlabeled spike-in RNAs was pooled and used for 4sU-seq.

788

789 **4sU-Seq**

790 Six million A549 WT or RLKO cells were seeded in 15cm tissue culture dishes and cultured
791 overnight before transfection. Then, cells were then transfected with poly(I:C) for 4 hours,

792 followed by pulse labeling with 500μM 4sU dissolved in DMEM media supplemented with 10%
793 FBS for 10 minutes. The plates were washed once with PBS, then lysed with 2ml TRIzol. RNA
794 was extracted from the TRIzol lysate, followed by isopropanol precipitation. 100μg or 300μg
795 (WT with poly(I:C)) total RNA was combined with an equal amount of pooled spike-in RNA
796 and was biotinylated with HPDP-biotin (Thermo Scientific cat # PI21341, 50μg per 25μg of
797 RNA) for 2 hours, followed by two chloroform extractions and isopropanol precipitation. The
798 RNA samples were denatured at 65°C for 5 minutes, then incubated with Dynabeads MyOne
799 Streptavidin C1 magnetic beads (Thermo Fisher, cat # 65002) that had been previously
800 blocked with glycogen for 1 hour. The beads were washed twice with wash buffer (100 mM
801 Tris-HCl, 10 mM EDTA, 1 M sodium chloride, and 0.1% Tween 20) at 65°C then twice at room
802 temperature. To increase the stringency of the washes, the beads were further washed with
803 TE buffer (10mM Tris-HCl pH 7.4, 1mM EDTA) twice at 55°C [70]. 4sU-RNA was then eluted from
804 the beads twice with 100 μL of 100 mM DTT, and the combined eluent was precipitated with
805 isopropanol.

806 The sequencing library was constructed using KAPA Stranded RNA-Seq Kit with RiboErase
807 (HMR) (cat # KK8484, 07962304001) and KAPA Single-Indexed Adapter Kit (Roche, cat #
808 KK8700, 08005699001) following manufacturer's instructions, with the following
809 modifications: Briefly, 60ng to 100ng RNA was used as input without rRNA depletion and
810 fragmented at 85 °C for 6 minutes; the PCR cycle numbers were determined empirically by
811 qPCR. The library was submitted to QB3-Berkeley Genomics Sequencing Core for QC and
812 sequencing on a NovaSeq 6000 S1 chip.

813

814 **Analysis of published RNA-seq datasets**

815 Published total RNA-seq datasets for mock- or poly(I:C)-transfected A549 cells (GEO:
816 GSE124144) [2] were used to as a proxy to assign the dominant transcript for each gene. The
817 raw fastq files were first pre-processed using HTStream (https://github.com/s4hts/HTStream)
818 then pseudo-aligned and quantified using Kallisto [71]. For each gene, the highest expressed
819 transcript (measured by transcript-per-million, TPM, first criteria) with the longest transcript

820 length (second criteria) was selected as the dominant transcript. Only genes on the main
821 nuclear chromosomes (i.e., chr1-22, chrX and chrY) and the corresponding dominant
822 transcript with average TPM > 0 are included.

823

824 **4sU-Seq data processing**

825 The raw reads were pre-processed using HTStream v1.3.2
826 (https://github.com/s4hts/HTStream), which included the separation of rRNA and non-rRNA
827 reads into separate files via HTStream SeqScreener. The rRNA reads were aligned to the
828 rDNA repeat (GenBank Accession U13369.1), concatenated with ERCC sequences, and the
829 non-rRNA reads were aligned to the human genome (hg38), concatenated with ERCC
830 sequences, using STAR v2.6.1b [56]. When aligning rRNA reads, options *--alignIntronMax 1* and
831 *--alignSJDBoverhangMin 999* were set to suppress gapped alignment. Aligned reads were
832 counted using Rsubread (v2.16.1) FeatureCounts [57], and differential gene expression
833 analysis was performed with limma-Voom v3.58.1, normalized to 4sU-labeled spike-in. [58]. A
834 model of ~0+group+replicate is used to account for batch effects. Segments of pre-rRNA (i.e.,
835 5' ETS, 18S, ITS1, 5.8S, ITS2, 28S, 3' ETS) were included in the differential expression analysis.
836 Scaled, stranded BigWig files were generated with Deeptools bamCoverage function, using
837 scaling factors generated in limma-Voom (proportional to the reciprocal of norm.factors ×
838 lib.sizes). BigWig files of biological replicates were averaged using Deeptools bigwigAverage
839 function. For both operations, bin sizes were set to 20bp. The metagene coverage plots were
840 generated using Deeptools [59] using the coordinates of dominant transcripts defined in
841 "Analysis of published RNA-seq datasets". GO term analysis was performed with the topGO
842 package (DOI: 10.18129/B9.bioc.topGO), using the Weight01 algorithm and Fisher's exact
843 test.

844

845 **CUT&RUN-sequencing**

846 The CUT&RUN procedure was performed according to previous reports [72,73], with
847 modifications. Briefly, 250,000 A549 WT or RNase L KO cells were seeded per well in a 12-
848 well plate and cultured overnight before transfection. Then cells were then transfected with
849 RNAiMAX alone or with 0.76 μg/ml poly(I:C) for 4 hours The cells were permeabilize on plate
850 with 500μL Perm buffer (20 mM HEPES-KOH pH 7.5, 150 mM NaCl, 0.5 mM Spermidine
851 (Sigma, S2626), 0.1% Triton X-100 (Sigma, X100), and proteinase inhibitor (Roche,
852 04693132001)) for 15 minutes at room temperature. The cells were washed again with Perm
853 buffer then incubated with either anti-Rpb1 S5P CTD (4H8, Cell Signaling, cat #2629) at 1: 50
854 dilution, equal mass of mouse normal IgG (Santa Cruz, cat # sc-2025), or anti-Rpb1 S2P CTD
855 (clone E1Z3G, Cell Signaling, cat # 13499) at 1: 50 dilution, in 200μL Perm buffer for 1 hour
856 at room temperature. The cells were then washed twice with Perm buffer and incubated with
857 pAG-MNase (Cell Signaling, cat #40366) at a 1:33 dilution in 200μL Perm buffer for 1 hour at
858 room temperature. The cells were then washed twice with Perm buffer and chilled on ice.
859 Then, 225 μL ice-cold Perm buffer containing 5 mM $CaCl_2$ was dispensed per well, and the
860 plate was incubated in a refrigerator at 4°C for 30 min for targeted digestion. The reaction
861 was halted by adding 75 μL 4× STOP solution (680 mM NaCl, 40 mM EDTA, 8 mM EGTA, 100
862 μg/ml RNase A (Invitrogen, cat # 12091021) and 0.1% Triton X-100, spiked with yeast genomic
863 DNA (Cell Signaling, cat #40366) at 10pg per sample for 4H8 and IgG, 30pg per sample for
864 E1Z3G). The plate was then incubated at 37°C for 30min to facilitate fragment release. The
865 supernatant was collected, and then 3μL 20% SDS solution and 3.75μL 20mg/ml proteinase
866 K solution were added. The mixture was then incubated at 50°C for 1 hour. The DNA was
867 extracted with phenol:chloroform.

868 The sequencing library was constructed with NEBNext® Ultra™ II DNA Library Prep Kit (NEB,
869 cat # E7645L) following a previous report [74] with modifications. Briefly, equal volume of
870 purified DNA fragments was used. End preparation was performed at 20°C for 30 min and
871 then at 50°C for 60 min to prevent short fragment melting. Fragments were then ligated to
872 adaptors from NEBNext® Multiplex Oligos for Illumina® (Unique Dual Index UMI Adaptors
873 DNA Set 1, NEB, cat # E7395S) and cleaned up twice with 1.1X Ampure XP beads (Beckman
874 Coutler, cat # A63880). The resulting ligated products were then PCR amplified for 10 cycles

875 for 4H8 and E1Z3G, and 14 cycles for IgG samples, respectively. The cycle numbers were
876 determined empirically by qPCR. The amplified libraries were double-sided size-selected
877 with 0.6X and 1.1X Ampure XP beads and further cleaned up by 1 round with 1.1X beads for
878 4H8, E1Z3G, or 3 rounds for IgG samples, to remove adaptor dimers. The libraries were
879 sequenced on AVITI platform (Element Biosciences) by UC Davis sequencing core.

880 **CUT&RUN data processing**

881 Reads were trimmed with Trimmomatic v0.39 [60] and aligned to a concatenated human (hg38)
882 and yeast (SacCer3) genome with bowtie 2 v2.5.2 [61]. The BAM files were then deduplicated
883 with UMI_tools v1.1.5 [63] and optionally splitted into subnucleosomal (<120bp) and
884 nucleosomal (>120bp) fractions using Deeptools (v3.5.5) alignmentSieve. The spike-in
885 normalization factors were calculated by counting reads mapped to yeast genome using
886 Samtools idxstats[62], followed by conversion to scaling factors that are proportional to the
887 reciprocal to the spike-in read counts. BigWig files were generated with Deeptools
888 bamCoverage function, using scaling factors generated above. BigWig files of biological
889 replicates were averaged using Deeptools bigwigAverage function. For both operations, bin
890 sizes were set to 20bp. The metagene coverage plots were generated using Deeptools.
891 Differential binding analysis was performed with DiffBind v3.12.0 [64] using the built-in spike-
892 in normalization function in *dba.normalize*. A model of ~0+group+replicate is used to
893 account for batch effects. For analysis in Figure 6, different windows were analyzed
894 separately to avoid merging of regions by diffBind. For elongation index calculation,
895 FeatureCounts was used to count reads mapped to either TSS (-500bp to +250bp) or gene
896 body (+250bp to TES). One pseudocount was then added to all regions. Reads were then
897 normalized using the spike-in scaling factors generated above. Only genes with >16
898 counts/kb at both the TSS and the gene body were kept for subsequent calculation.
899 Elongation index was averaged by taking the geometric mean of 3 replicates, followed by
900 logarithmic conversion.

901

902 **Quantitative reverse transcription PCR (RT-qPCR)**

903 500,000 A549 WT or RLKO cells per well were seeded in 6-well plates the day before either
904 mock-transfecting or transfecting with 0.76μg/ml poly(I:C), in the absence or in the presence
905 of 1X brefeldin A (eBiosciences, cat # 00-4506-51) when indicated, for 3 hours. RNA samples
906 were prepared by TRIzol extraction. They were then treated with Turbo DNase (Thermo Fisher,
907 cat # AM2238) for 30 minutes at 37°C and re-purified by phenol:chloroform extraction. 500ng
908 to 1μg RNA was used for reverse transcription using AMV-RT (Promega, cat # M5108) and
909 random 9-mer primer (IDT). cDNA was then quantified by qPCR using iTaq Universal SYBR
910 Mastermix (Bio-Rad, cat # 1725125) and the indicated primer pairs. Transcript levels were
911 normalized to 18S.

912 For Figure S2B, an equal volume of 4sU RNA eluent was directly reverse-transcribed using
913 AMV-RT (Promega) and a random 9-mer primer (IDT), and quantified as above with the
914 indicated primer pairs. Transcript levels were normalized to spike-in.

915 For Figure 7B, 1μg RNA was treated with Turbo DNase for 15 minutes at 37°C and inactivated
916 at 70°C in the presence of 15mM EDTA. The treated RNA was diluted with DEPC water to 50μL
917 and 4μL was used for reverse transcription using AMV-RT and random 9-mer primer. cDNA
918 was then quantified by qPCR with iTaq Universal SYBR Mastermix.

919

920 **Western blotting**

921 To prepare whole-cell lysates for evaluating RNase L knock-down, murine iBMDMs
922 transfected with RNase L targeting siRNAs (Horizon, cat # L-043480-00-0010) were washed
923 with cold DPBS (Gibco) followed by lysis with radioimmunoprecipitation assay (RIPA) lysis
924 buffer (50 mM Tris HCl, 150 mM NaCl, 1.0% [vol/vol] NP-40, 0.5% [wt/vol] sodium
925 deoxycholate, 1.0 mM EDTA, and 1% [wt/vol] SDS, Halt™ Protease and Phosphatase Inhibitor
926 Cocktail (Thermo Fisher, cat # PI78440). Cell lysates were vortexed briefly, rotated at 4°C for
927 15 min, and then clarified by centrifugation at 21,000 × *g* in a tabletop centrifuge at 4°C for
928 10 min to remove debris. 30 μg of whole-cell lysate were resolved on 4% to 15% mini-
929 PROTEAN TGX gels (Bio-Rad). Transfers to polyvinylidene difluoride (PVDF) membranes (Bio-
930 Rad) were done with the Trans-Blot Turbo transfer system (Bio-Rad). Blots were incubated in

931 5% milk in TBS with 0.1% Tween 20 (TBS-T) to block, followed by incubation with primary
932 antibodies against anti-RNase L (Abcam, ab191392, 1:10,000) and anti-GAPDH antibody
933 (abcam ab8245, 1;5,000). Washes were carried out with TBS-T. Blots were then incubated
934 with HRP-conjugated secondary antibodies (Southern Biotechnology, 1:5,000). Washed
935 blots were incubated with Clarity Western ECL substrate (Bio-Rad) for 5 min and visualized
936 with a ChemiDoc imager (Bio-Rad). Band intensity was analyzed with ImageJ [66].

937

938 QUANTIFICATION AND STATISTICAL ANALYSIS

939 All statistical analyses were performed with GraphPad Prism 10 and RStudio. For limma-
940 Voom analysis for 4sU-seq, and DiffBind analysis for CUT&RUN-seq, adjusted P value or
941 False discovery rate (FDR) is corrected with the Benjamini-Hochberg (BH) method. All
942 statistical method details and the p value notation are included in figure legends.

943

944

945 **Video S1-S4**. **Related to Figure 4.** Z-stack movies showing the localization of POLR1A (left
946 panel) and NPM1 (center panel) or the merged view (right panel) in mock-treated WT (*video*
947 *S1*) or RLKO (*video S2*) A549 cells or p(I:C)-treated WT (*video S3*) or RLKO (*video S4*) A549
948 cells.

949 **Supplemental Table 1.** Primer sequences used in this study.

950

References

1. Karasik, A., and Guydosh, N.R. (2024). The Unusual Role of Ribonuclease L in Innate Immunity. Wiley Interdiscip Rev RNA *15*, e1878. 10.1002/wrna.1878.
2. Burke, J.M., Moon, S.L., Matheny, T., and Parker, R. (2019). RNase L Reprograms Translation by Widespread mRNA Turnover Escaped by Antiviral mRNAs. Mol Cell *75*, 1203-1217 e1205. 10.1016/j.molcel.2019.07.029.
3. Donovan, J., Rath, S., Kolet-Mandrikov, D., and Korennykh, A. (2017). Rapid RNase L-driven arrest of protein synthesis in the dsRNA response without degradation of translation machinery. RNA *23*, 1660-1671. 10.1261/rna.062000.117.
4. Rath, S., Prangley, E., Donovan, J., Demarest, K., Wingreen, N.S., Meir, Y., and Korennykh, A. (2019). Concerted 2-5A-Mediated mRNA Decay and Transcription Reprogram Protein Synthesis in the dsRNA Response. Mol Cell *75*, 1218-1228 e1216. 10.1016/j.molcel.2019.07.027.
5. Chitrakar, A., Rath, S., Donovan, J., Demarest, K., Li, Y., Sridhar, R.R., Weiss, S.R., Kotenko, S.V., Wingreen, N.S., and Korennykh, A. (2019). Real-time 2-5A kinetics suggest that interferons beta and lambda evade global arrest of translation by RNase L. Proc Natl Acad Sci U S A *116*, 2103-2111. 10.1073/pnas.1818363116.
6. Burke, J.M., Gilchrist, A.R., Sawyer, S.L., and Parker, R. (2021). RNase L limits host and viral protein synthesis via inhibition of mRNA export. Sci Adv *7*. 10.1126/sciadv.abh2479.
7. Burke, J.M., Ripin, N., Ferretti, M.B., St Clair, L.A., Worden-Sapper, E.R., Salgado, F., Sawyer, S.L., Perera, R., Lynch, K.W., and Parker, R. (2022). RNase L activation in the cytoplasm induces aberrant processing of mRNAs in the nucleus. PLoS Pathog *18*, e1010930. 10.1371/journal.ppat.1010930.
8. Karasik, A., Lorenzi, H.A., DePass, A.V., and Guydosh, N.R. (2024). Endonucleolytic RNA cleavage drives changes in gene expression during the innate immune response. Cell Rep *43*, 114287. 10.1016/j.celrep.2024.114287.
9. Lee, D., Le Pen, J., Yatim, A., Dong, B., Aquino, Y., Ogishi, M., Pescarmona, R., Talouarn, E., Rinchai, D., Zhang, P., et al. (2023). Inborn errors of OAS-RNase L in SARS-CoV-2-related multisystem inflammatory syndrome in children. Science *379*, eabo3627. 10.1126/science.abo3627.
10. Malathi, K., Dong, B., Gale, M., Jr., and Silverman, R.H. (2007). Small self-RNA generated by RNase L amplifies antiviral innate immunity. Nature *448*, 816-819. 10.1038/nature06042.
11. Xi, J., Snieckute, G., Martinez, J.F., Arendrup, F.S.W., Asthana, A., Gaughan, C., Lund, A.H., Bekker-Jensen, S., and Silverman, R.H. (2024). Initiation of a ZAKalpha-dependent ribotoxic stress response by the innate immunity endoribonuclease RNase L. Cell Rep *43*, 113998. 10.1016/j.celrep.2024.113998.
12. Yang, K., Dong, B., Asthana, A., Silverman, R.H., and Yan, N. (2024). RNA helicase SKIV2L limits antiviral defense and autoinflammation elicited by the OAS-RNase L pathway. EMBO J *43*, 3876-3894. 10.1038/s44318-024-00187-1.

13. Banerjee, S., Chakrabarti, A., Jha, B.K., Weiss, S.R., and Silverman, R.H. (2014). Cell-type-specific effects of RNase L on viral induction of beta interferon. mBio *5*, e00856-00814. 10.1128/mBio.00856-14.
14. Iordanov, M.S., Paranjape, J.M., Zhou, A., Wong, J., Williams, B.R., Meurs, E.F., Silverman, R.H., and Magun, B.E. (2000). Activation of p38 mitogen-activated protein kinase and c-Jun NH(2)-terminal kinase by double-stranded RNA and encephalomyocarditis virus: involvement of RNase L, protein kinase R, and alternative pathways. Mol Cell Biol *20*, 617-627. 10.1128/MCB.20.2.617-627.2000.
15. Lee, Y.J., and Glaunsinger, B.A. (2009). Aberrant herpesvirus-induced polyadenylation correlates with cellular messenger RNA destruction. PLoS Biol *7*, e1000107. 10.1371/journal.pbio.1000107.
16. Kumar, G.R., and Glaunsinger, B.A. (2010). Nuclear import of cytoplasmic poly(A) binding protein restricts gene expression via hyperadenylation and nuclear retention of mRNA. Mol Cell Biol *30*, 4996-5008. 10.1128/MCB.00600-10.
17. Kumar, G.R., Shum, L., and Glaunsinger, B.A. (2011). Importin alpha-mediated nuclear import of cytoplasmic poly(A) binding protein occurs as a direct consequence of cytoplasmic mRNA depletion. Mol Cell Biol *31*, 3113-3125. 10.1128/MCB.05402-11.
18. Gaglia, M.M., Covarrubias, S., Wong, W., and Glaunsinger, B.A. (2012). A common strategy for host RNA degradation by divergent viruses. J Virol *86*, 9527-9530. 10.1128/JVI.01230-12.
19. Abernathy, E., Gilbertson, S., Alla, R., and Glaunsinger, B. (2015). Viral Nucleases Induce an mRNA Degradation-Transcription Feedback Loop in Mammalian Cells. Cell Host Microbe *18*, 243-253. 10.1016/j.chom.2015.06.019.
20. Gilbertson, S., Federspiel, J.D., Hartenian, E., Cristea, I.M., and Glaunsinger, B. (2018). Changes in mRNA abundance drive shuttling of RNA binding proteins, linking cytoplasmic RNA degradation to transcription. Elife *7*. 10.7554/eLife.37663.
21. Hartenian, E., Gilbertson, S., Federspiel, J.D., Cristea, I.M., and Glaunsinger, B.A. (2020). RNA decay during gammaherpesvirus infection reduces RNA polymerase II occupancy of host promoters but spares viral promoters. PLoS Pathog *16*, e1008269. 10.1371/journal.ppat.1008269.
22. Thomas, M.P., Liu, X., Whangbo, J., McCrossan, G., Sanborn, K.B., Basar, E., Walch, M., and Lieberman, J. (2015). Apoptosis Triggers Specific, Rapid, and Global mRNA Decay with 3' Uridylated Intermediates Degraded by DIS3L2. Cell Rep *11*, 1079-1089. 10.1016/j.celrep.2015.04.026.
23. Liu, X., Fu, R., Pan, Y., Meza-Sosa, K.F., Zhang, Z., and Lieberman, J. (2018). PNPT1 Release from Mitochondria during Apoptosis Triggers Decay of Poly(A) RNAs. Cell *174*, 187-201 e112. 10.1016/j.cell.2018.04.017.
24. Duncan-Lewis, C., Hartenian, E., King, V., and Glaunsinger, B.A. (2021). Cytoplasmic mRNA decay represses RNA polymerase II transcription during early apoptosis. Elife *10*. 10.7554/eLife.58342.
25. Siddiqui, M.A., and Malathi, K. (2012). RNase L induces autophagy via c-Jun N-terminal kinase and double-stranded RNA-dependent protein kinase signaling pathways. J Biol Chem *287*, 43651-43664. 10.1074/jbc.M112.399964.

1036 26. Watkins, J.M., and Burke, J.M. (2024). RNase L-induced bodies sequester
1037 subgenomic flavivirus RNAs to promote viral RNA decay. Cell Rep *43*, 114694.
1038 10.1016/j.celrep.2024.114694.
1039 27. Whelan, J.N., Li, Y., Silverman, R.H., and Weiss, S.R. (2019). Zika Virus Production Is
1040 Resistant to RNase L Antiviral Activity. J Virol *93*. 10.1128/JVI.00313-19.
1041 28. Whelan, J.N., Parenti, N.A., Hatterschide, J., Renner, D.M., Li, Y., Reyes, H.M., Dong,
1042 B., Perez, E.R., Silverman, R.H., and Weiss, S.R. (2021). Zika virus employs the host
1043 antiviral RNase L protein to support replication factory assembly. Proc Natl Acad Sci
1044 U S A *118*. 10.1073/pnas.2101713118.
1045 29. Slomnicki, L.P., Chung, D.H., Parker, A., Hermann, T., Boyd, N.L., and Hetman, M.
1046 (2017). Ribosomal stress and Tp53-mediated neuronal apoptosis in response to
1047 capsid protein of the Zika virus. Sci Rep *7*, 16652. 10.1038/s41598-017-16952-8.
1048 30. Berry, S., Muller, M., Rai, A., and Pelkmans, L. (2022). Feedback from nuclear RNA
1049 on transcription promotes robust RNA concentration homeostasis in human cells.
1050 Cell Syst *13*, 454-470 e415. 10.1016/j.cels.2022.04.005.
1051 31. Radle, B., Rutkowski, A.J., Ruzsics, Z., Friedel, C.C., Koszinowski, U.H., and Dolken,
1052 L. (2013). Metabolic labeling of newly transcribed RNA for high resolution gene
1053 expression profiling of RNA synthesis, processing and decay in cell culture. J Vis Exp.
1054 10.3791/50195.
1055 32. Andersen, J.B., Mazan-Mamczarz, K., Zhan, M., Gorospe, M., and Hassel, B.A.
1056 (2009). Ribosomal protein mRNAs are primary targets of regulation in RNase-L-
1057 induced senescence. RNA Biol *6*, 305-315. 10.4161/rna.6.3.8526.
1058 33. Shore, D., and Albert, B. (2022). Ribosome biogenesis and the cellular energy
1059 economy. Curr Biol *32*, R611-R617. 10.1016/j.cub.2022.04.083.
1060 34. Niu, T.K., Pfeifer, A.C., Lippincott-Schwartz, J., and Jackson, C.L. (2005). Dynamics
1061 of GBF1, a Brefeldin A-sensitive Arf1 exchange factor at the Golgi. Mol Biol Cell *16*,
1062 1213-1222. 10.1091/mbc.e04-07-0599.
1063 35. Cusic, R., and Burke, J.M. (2024). Condensation of RNase L promotes its rapid
1064 activation in response to viral infection in mammalian cells. Sci Signal *17*, eadi9844.
1065 10.1126/scisignal.adi9844.
1066 36. Zhu, Z., Liu, J., Feng, H., Zhang, Y., Huang, R., Pan, Q., Nan, J., Miao, R., and Cheng,
1067 B. (2022). Overcoming the cytoplasmic retention of GDOWN1 modulates global
1068 transcription and facilitates stress adaptation. Elife *11*. 10.7554/eLife.79116.
1069 37. Hoboth, P., Sztacho, M., and Hozak, P. (2024). Nuclear patterns of
1070 phosphatidylinositol 4,5- and 3,4-bisphosphate revealed by super-resolution
1071 microscopy differ between the consecutive stages of RNA polymerase II
1072 transcription. FEBS J *291*, 4240-4264. 10.1111/febs.17136.
1073 38. Fan, Z., Devlin, J.R., Hogg, S.J., Doyle, M.A., Harrison, P.F., Todorovski, I., Cluse, L.A.,
1074 Knight, D.A., Sandow, J.J., Gregory, G., et al. (2020). CDK13 cooperates with CDK12
1075 to control global RNA polymerase II processivity. Sci Adv *6*. 10.1126/sciadv.aaz5041.
1076 39. Gu, B., Eick, D., and Bensaude, O. (2013). CTD serine-2 plays a critical role in
1077 splicing and termination factor recruitment to RNA polymerase II in vivo. Nucleic
1078 Acids Res *41*, 1591-1603. 10.1093/nar/gks1327.

40. Harlen, K.M., and Churchman, L.S. (2017). The code and beyond: transcription regulation by the RNA polymerase II carboxy-terminal domain. Nat Rev Mol Cell Biol *18*, 263-273. 10.1038/nrm.2017.10.
41. Vercruysse, T., Vanstreels, E., Jacquemyn, M., Boland, S., Kilonda, A., Allasia, S., Vandecaetsbeek, I., Klaassen, H., Versele, M., Chaltin, P., et al. (2024). Ibetazol, a novel inhibitor of importin beta1-mediated nuclear import. Commun Biol *7*, 1560. 10.1038/s42003-024-07237-8.
42. Aoi, Y., Iravani, L., Mroczek, I.C., Gold, S., Howard, B.C., and Shilatifard, A. (2025). SPT5 regulates RNA polymerase II stability via Cullin 3-ARMC5 recognition. Sci Adv *11*, eadt5885. 10.1126/sciadv.adt5885.
43. Blears, D., Lou, J., Fong, N., Mitter, R., Sheridan, R.M., He, D., Dirac-Svejstrup, A.B., Bentley, D., and Svejstrup, J.Q. (2024). Redundant pathways for removal of defective RNA polymerase II complexes at a promoter-proximal pause checkpoint. Mol Cell *84*, 4790-4807 e4711. 10.1016/j.molcel.2024.10.012.
44. Cacioppo, R., Gillis, A., Shlamovitz, I., Zeller, A., Castiblanco, D., Crisp, A., Haworth, B., Arabiotorre, A., Abyaneh, P., Bao, Y., et al. (2024). CRL3(ARMC5) ubiquitin ligase and Integrator phosphatase form parallel mechanisms to control early stages of RNA Pol II transcription. Mol Cell *84*, 4808-4823 e4813. 10.1016/j.molcel.2024.11.024.
45. Potapova, T.A., Unruh, J.R., Conkright-Fincham, J., Banks, C.A.S., Florens, L., Schneider, D.A., and Gerton, J.L. (2023). Distinct states of nucleolar stress induced by anticancer drugs. Elife *12*. 10.7554/eLife.88799.
46. Williams, T.D., Michalak, E.M., Carey, K.T., Lam, E.Y.N., Anderson, A., Griesbach, E., Chan, Y.C., Papasaikas, P., Tan, V.W.T., Ngo, L., et al. (2025). mRNA export factors store nascent transcripts within nuclear speckles as an adaptive response to transient global inhibition of transcription. Mol Cell *85*, 117-131 e117. 10.1016/j.molcel.2024.12.008.
47. Kim, J., Han, K.Y., Khanna, N., Ha, T., and Belmont, A.S. (2019). Nuclear speckle fusion via long-range directional motion regulates speckle morphology after transcriptional inhibition. J Cell Sci *132*. 10.1242/jcs.226563.
48. Decker, C.J., Burke, J.M., Mulvaney, P.K., and Parker, R. (2022). RNA is required for the integrity of multiple nuclear and cytoplasmic membrane-less RNP granules. EMBO J *41*, e110137. 10.15252/embj.2021110137.
49. Aprile-Garcia, F., Tomar, P., Hummel, B., Khavaran, A., and Sawarkar, R. (2019). Nascent-protein ubiquitination is required for heat shock-induced gene downregulation in human cells. Nat Struct Mol Biol *26*, 137-146. 10.1038/s41594-018-0182-x.
50. Bulut-Karslioglu, A., Macrae, T.A., Oses-Prieto, J.A., Covarrubias, S., Percharde, M., Ku, G., Diaz, A., McManus, M.T., Burlingame, A.L., and Ramalho-Santos, M. (2018). The Transcriptionally Permissive Chromatin State of Embryonic Stem Cells Is Acutely Tuned to Translational Output. Cell Stem Cell *22*, 369-383 e368. 10.1016/j.stem.2018.02.004.

51. Takenaka, Y., Yamada, A., Tomioka, Y., Akiyama, Y., and Ivanov, P. (2025). RNase L Produces tRNA-derived RNAs that Contribute to Translation Inhibition. RNA. 10.1261/rna.080419.125.
52. Huai, W., Yang, K., Xing, C., Song, K., Lyu, H., Williams, N.S., Wu, J., and Yan, N. (2025). OAS cross-activates RNase L intercellularly through cell-to-cell transfer of 2-5A to spread innate immunity. Immunity *58*, 797-810 e796. 10.1016/j.immuni.2025.01.016.
53. Balsitis, S.J., Coloma, J., Castro, G., Alava, A., Flores, D., McKerrow, J.H., Beatty, P.R., and Harris, E. (2009). Tropism of dengue virus in mice and humans defined by viral nonstructural protein 3-specific immunostaining. Am J Trop Med Hyg *80*, 416-424.
54. Tabata, T., Petitt, M., Puerta-Guardo, H., Michlmayr, D., Wang, C., Fang-Hoover, J., Harris, E., and Pereira, L. (2016). Zika Virus Targets Different Primary Human Placental Cells, Suggesting Two Routes for Vertical Transmission. Cell Host Microbe *20*, 155-166. 10.1016/j.chom.2016.07.002.
55. Robinson, E.K., Jagannatha, P., Covarrubias, S., Cattle, M., Smaliy, V., Safavi, R., Shapleigh, B., Abu-Shumays, R., Jain, M., Cloonan, S.M., et al. (2021). Inflammation drives alternative first exon usage to regulate immune genes including a novel iron-regulated isoform of Aim2. Elife *10*. 10.7554/eLife.69431.
56. Dobin, A., Davis, C.A., Schlesinger, F., Drenkow, J., Zaleski, C., Jha, S., Batut, P., Chaisson, M., and Gingeras, T.R. (2013). STAR: ultrafast universal RNA-seq aligner. Bioinformatics *29*, 15-21. 10.1093/bioinformatics/bts635.
57. Liao, Y., Smyth, G.K., and Shi, W. (2014). featureCounts: an efficient general purpose program for assigning sequence reads to genomic features. Bioinformatics *30*, 923-930. 10.1093/bioinformatics/btt656.
58. Ritchie, M.E., Phipson, B., Wu, D., Hu, Y., Law, C.W., Shi, W., and Smyth, G.K. (2015). limma powers differential expression analyses for RNA-sequencing and microarray studies. Nucleic Acids Res *43*, e47. 10.1093/nar/gkv007.
59. Ramirez, F., Ryan, D.P., Gruning, B., Bhardwaj, V., Kilpert, F., Richter, A.S., Heyne, S., Dundar, F., and Manke, T. (2016). deepTools2: a next generation web server for deep-sequencing data analysis. Nucleic Acids Res *44*, W160-165. 10.1093/nar/gkw257.
60. Bolger, A.M., Lohse, M., and Usadel, B. (2014). Trimmomatic: a flexible trimmer for Illumina sequence data. Bioinformatics *30*, 2114-2120. 10.1093/bioinformatics/btu170.
61. Langmead, B., and Salzberg, S.L. (2012). Fast gapped-read alignment with Bowtie 2. Nat Methods *9*, 357-359. 10.1038/nmeth.1923.
62. Li, H., Handsaker, B., Wysoker, A., Fennell, T., Ruan, J., Homer, N., Marth, G., Abecasis, G., Durbin, R., and Genome Project Data Processing, S. (2009). The Sequence Alignment/Map format and SAMtools. Bioinformatics *25*, 2078-2079. 10.1093/bioinformatics/btp352.
63. Smith, T., Heger, A., and Sudbery, I. (2017). UMI-tools: modeling sequencing errors in Unique Molecular Identifiers to improve quantification accuracy. Genome Res *27*, 491-499. 10.1101/gr.209601.116.

64. Ross-Innes, C.S., Stark, R., Teschendorff, A.E., Holmes, K.A., Ali, H.R., Dunning, M.J., Brown, G.D., Gojis, O., Ellis, I.O., Green, A.R., et al. (2012). Differential oestrogen receptor binding is associated with clinical outcome in breast cancer. Nature *481*, 389-393. 10.1038/nature10730.
65. Schindelin, J., Arganda-Carreras, I., Frise, E., Kaynig, V., Longair, M., Pietzsch, T., Preibisch, S., Rueden, C., Saalfeld, S., Schmid, B., et al. (2012). Fiji: an open-source platform for biological-image analysis. Nat Methods *9*, 676-682. 10.1038/nmeth.2019.
66. Schneider, C.A., Rasband, W.S., and Eliceiri, K.W. (2012). NIH Image to ImageJ: 25 years of image analysis. Nat Methods *9*, 671-675. 10.1038/nmeth.2089.
67. Sancak, Y., Peterson, T.R., Shaul, Y.D., Lindquist, R.A., Thoreen, C.C., Bar-Peled, L., and Sabatini, D.M. (2008). The Rag GTPases bind raptor and mediate amino acid signaling to mTORC1. Science *320*, 1496-1501. 10.1126/science.1157535.
68. Chiu, J., March, P.E., Lee, R., and Tillett, D. (2004). Site-directed, Ligase-Independent Mutagenesis (SLIM): a single-tube methodology approaching 100% efficiency in 4 h. Nucleic Acids Res *32*, e174. 10.1093/nar/gnh172.
69. Schwalb, B., Michel, M., Zacher, B., Fruhauf, K., Demel, C., Tresch, A., Gagneur, J., and Cramer, P. (2016). TT-seq maps the human transient transcriptome. Science *352*, 1225-1228. 10.1126/science.aad9841.
70. Li, H.B., Tong, J., Zhu, S., Batista, P.J., Duffy, E.E., Zhao, J., Bailis, W., Cao, G., Kroehling, L., Chen, Y., et al. (2017). m(6)A mRNA methylation controls T cell homeostasis by targeting the IL-7/STAT5/SOCS pathways. Nature *548*, 338-342. 10.1038/nature23450.
71. Bray, N.L., Pimentel, H., Melsted, P., and Pachter, L. (2016). Near-optimal probabilistic RNA-seq quantification. Nat Biotechnol *34*, 525-527. 10.1038/nbt.3519.
72. Miura, M., and Chen, H. (2020). CUT&RUN detects distinct DNA footprints of RNA polymerase II near the transcription start sites. Chromosome Res *28*, 381-393. 10.1007/s10577-020-09643-0.
73. Morgens, D.W., Gulyas, L., Mao, X., Rivera-Madera, A., Souza, A.S., and Glaunsinger, B.A. (2025). Enhancers and genome conformation provide complex transcriptional control of a herpesviral gene. Mol Syst Biol *21*, 30-58. 10.1038/s44320-024-00075-0.
74. Liu, N., Hargreaves, V.V., Zhu, Q., Kurland, J.V., Hong, J., Kim, W., Sher, F., Macias-Trevino, C., Rogers, J.M., Kurita, R., et al. (2018). Direct Promoter Repression by BCL11A Controls the Fetal to Adult Hemoglobin Switch. Cell *173*, 430-442 e417. 10.1016/j.cell.2018.03.016.

Figure 1

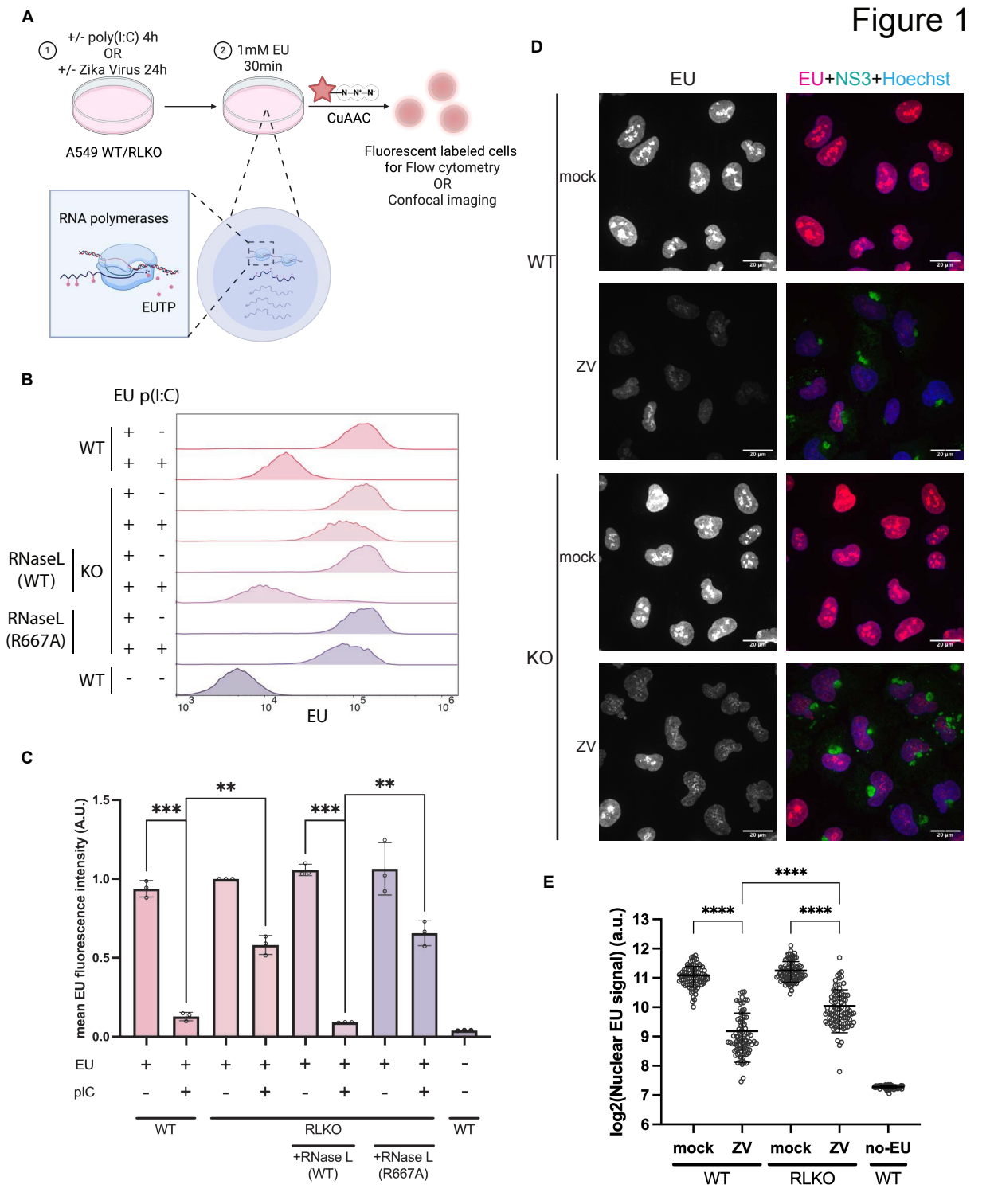
A
① +/- poly(I:C) 4h
OR
+/- Zika Virus 24h
② 1mM EU
30min
CuAAC
A549 WT/RLKO
Fluorescent labeled cells
for Flow cytometry
OR
Confocal imaging
RNA polymerases
EUTP
B
EU p(I:C)
WT
RNaseL (WT)
KO
RNaseL (R667A)
WT
EU
C
mean EU fluorescence intensity (A.U.)
EU
pIC
WT
RLKO
+RNase L (WT)
+RNase L (R667A)
WT
D
EU
EU+NS3+Hoechst
mock
ZV
WT
KO
E
log2(Nuclear EU signal) (a.u.)
mock
ZV
mock
ZV
no-EU
WT
RLKO
WT

Figure 2

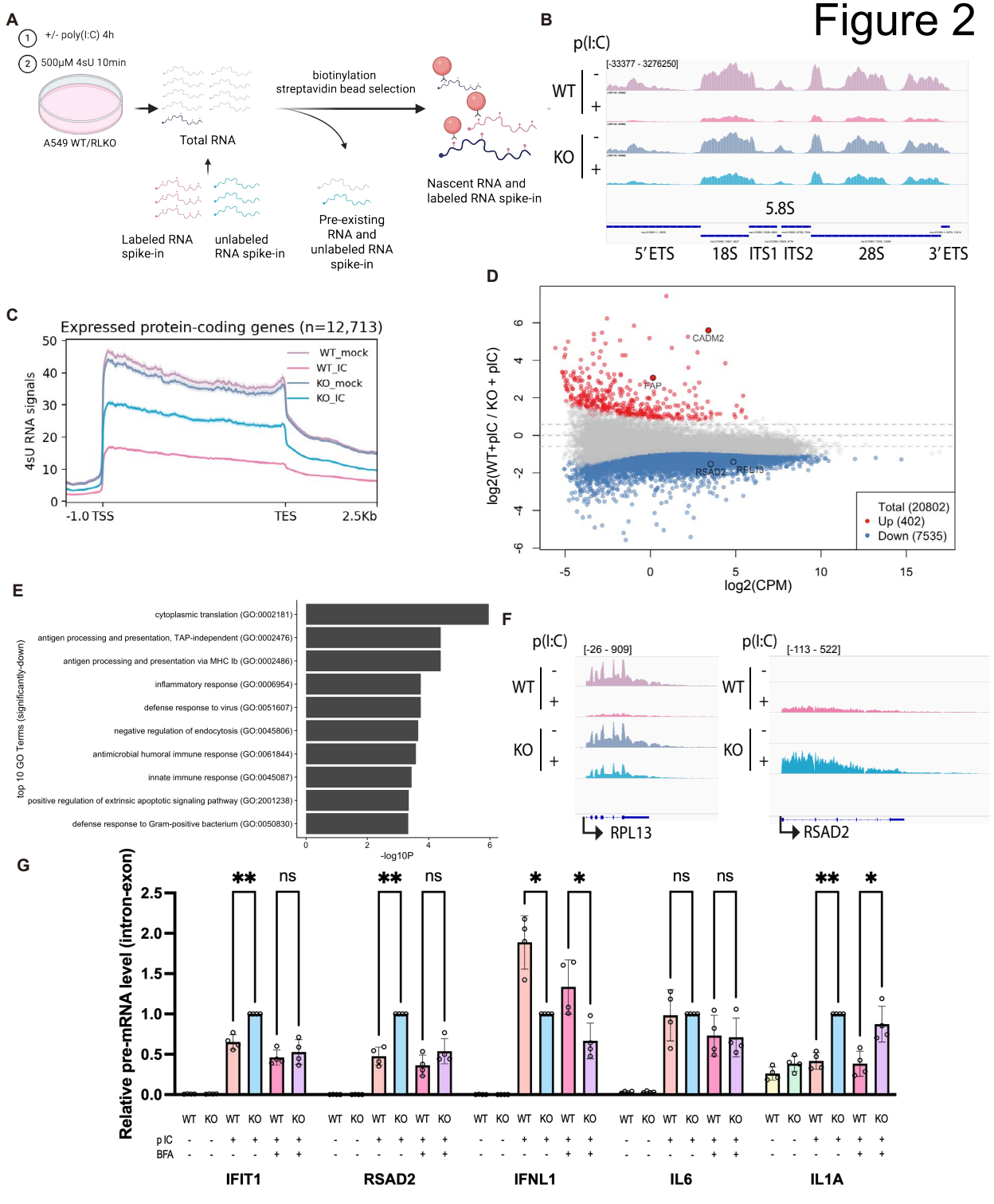
A
1 +/- poly(I:C) 4h
2 500μM 4sU 10min
A549 WT/RLKO
Total RNA
biotinylation
streptavidin bead selection
Nascent RNA and labeled RNA spike-in
Labeled RNA spike-in
unlabeled RNA spike-in
Pre-existing RNA and unlabeled RNA spike-in
B
p(I:C)
[-33377 - 3276250]
WT
KO
5.8S
5'ETS
18S
ITS1
ITS2
28S
3'ETS
C
Expressed protein-coding genes (n=12,713)
4sU RNA signals
WT_mock
WT_IC
KO_mock
KO_IC
-1.0 TSS
TES
2.5Kb
D
log2(WT+pIC / KO + pIC)
log2(CPM)
CADM2
PAP
RSAD2
RPL13
Total (20802)
Up (402)
Down (7535)
E
top 10 GO Terms (significantly-down)
cytoplasmic translation (GO:0002181)
antigen processing and presentation, TAP-independent (GO:0002476)
antigen processing and presentation via MHC Ib (GO:0002486)
inflammatory response (GO:0006954)
defense response to virus (GO:0051607)
negative regulation of endocytosis (GO:0045806)
antimicrobial humoral immune response (GO:0061844)
innate immune response (GO:0045087)
positive regulation of extrinsic apoptotic signaling pathway (GO:2001238)
defense response to Gram-positive bacterium (GO:0050830)
-log10P
F
p(I:C)
[-26 - 909]
[-113 - 522]
RPL13
RSAD2
G
Relative pre-mRNA level (intron-exon)
pIC
BFA
IFIT1
RSAD2
IFNL1
IL6
IL1A

Figure 3

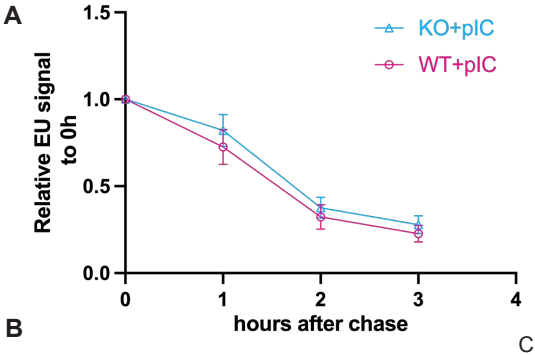
A
KO+pIC
WT+pIC
Relative EU signal to 0h
hours after chase

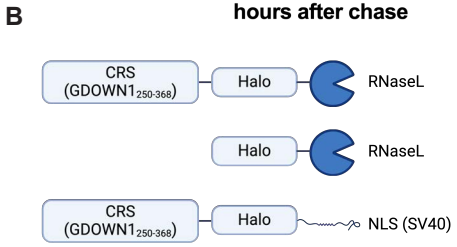
B
CRS (GDOWN1 250-368)
Halo
RNaseL
Halo
RNaseL
CRS (GDOWN1 250-368)
Halo
NLS (SV40)

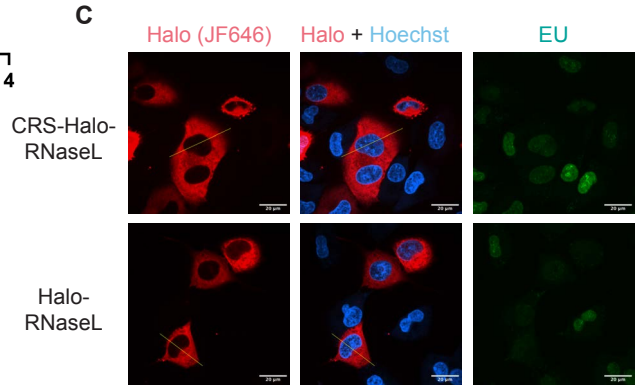
C
Halo (JF646)
Halo + Hoechst
EU
CRS-Halo-RNaseL
Halo-RNaseL

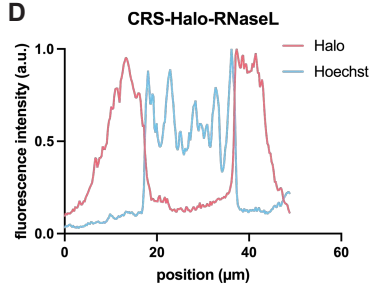
D
CRS-Halo-RNaseL
Halo
Hoechst
fluorescence intensity (a.u.)
position (µm)

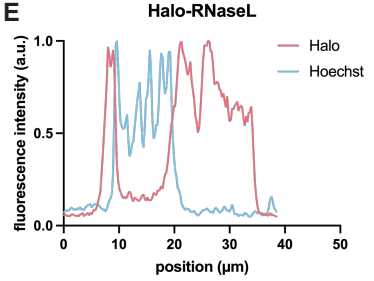
E
Halo-RNaseL
Halo
Hoechst
fluorescence intensity (a.u.)
position (µm)

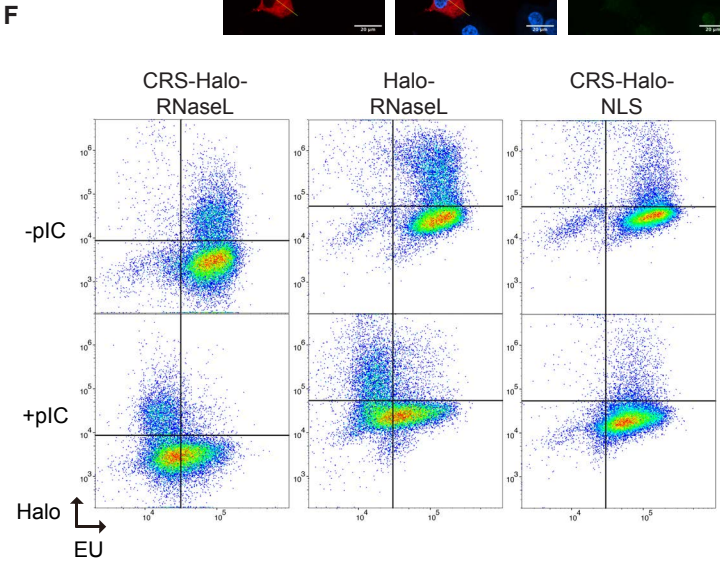
F
CRS-Halo-RNaseL
Halo-RNaseL
CRS-Halo-NLS
-pIC
+pIC
Halo
EU

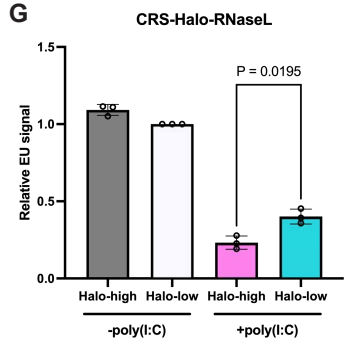
G
CRS-Halo-RNaseL
P = 0.0195
Relative EU signal
Halo-high
Halo-low
Halo-high
Halo-low
-poly(I:C)
+poly(I:C)

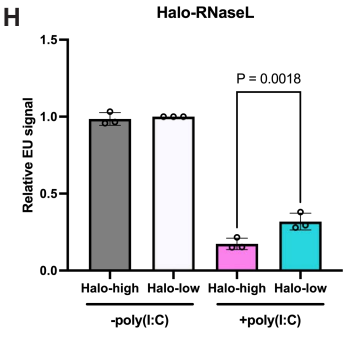
H
Halo-RNaseL
P = 0.0018
Relative EU signal
Halo-high
Halo-low
Halo-high
Halo-low
-poly(I:C)
+poly(I:C)

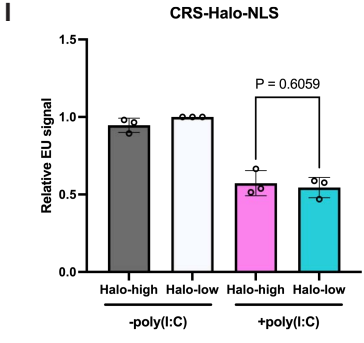
I
CRS-Halo-NLS
P = 0.6059
Relative EU signal
Halo-high
Halo-low
Halo-high
Halo-low
-poly(I:C)
+poly(I:C)

Figure 4

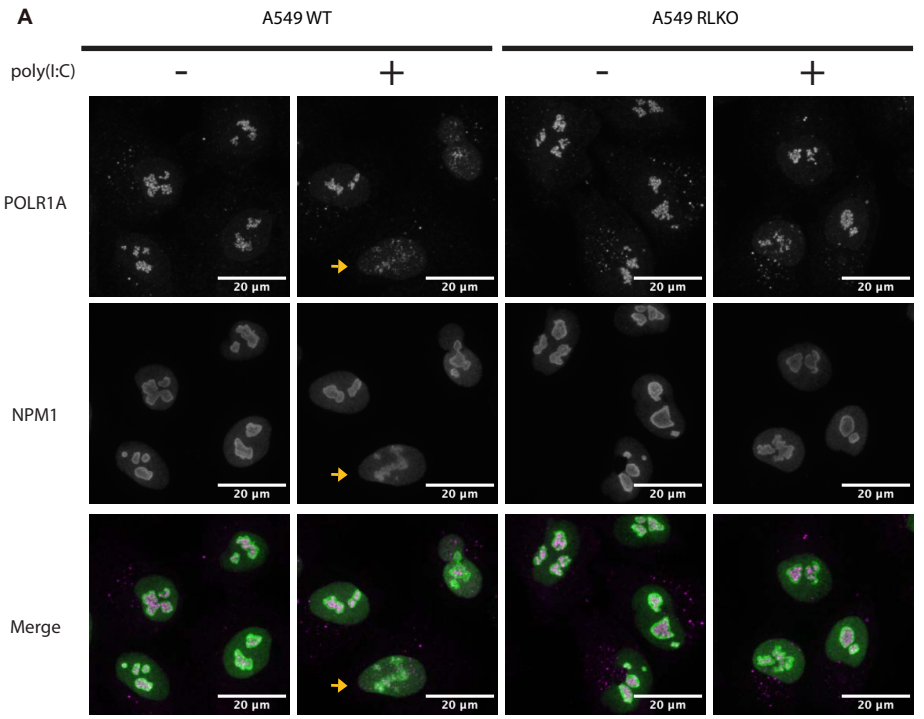
A
A549 WT
A549 RLKO
poly(I:C)
-
+
-
+
POLR1A
NPM1
Merge
20 µm

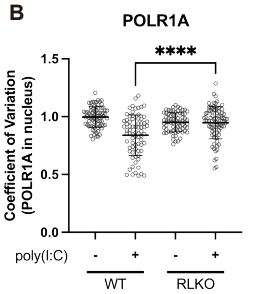
B
POLR1A
****
Coefficient of Variation (POLR1A in nucleus)
1.5
1.0
0.5
0.0
poly(I:C)
-
+
-
+
WT
RLKO

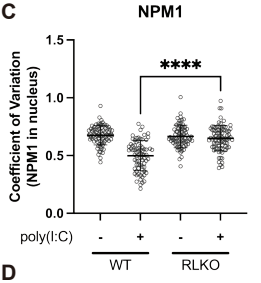
C
NPM1
****
Coefficient of Variation (NPM1 in nucleus)
1.5
1.0
0.5
0.0
poly(I:C)
-
+
-
+
WT
RLKO

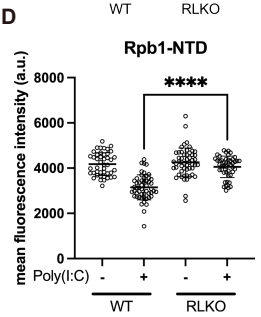
D
Rpb1-NTD
****
mean fluorescence intensity (a.u.)
8000
6000
4000
2000
0
Poly(I:C)
-
+
-
+
WT
RLKO

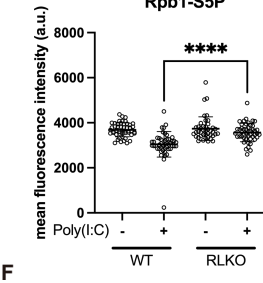
E
Rpb1-S5P
****
mean fluorescence intensity (a.u.)
8000
6000
4000
2000
0
Poly(I:C)
-
+
-
+
WT
RLKO

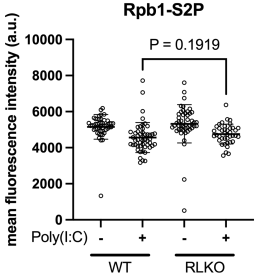
F
Rpb1-S2P
P = 0.1919
mean fluorescence intensity (a.u.)
10000
8000
6000
4000
2000
0
Poly(I:C)
-
+
-
+
WT
RLKO

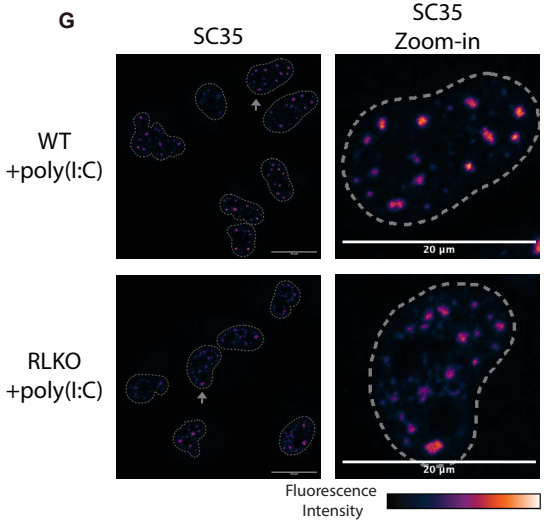
G
SC35
SC35 Zoom-in
WT +poly(I:C)
RLKO +poly(I:C)
20 µm
Fluorescence Intensity

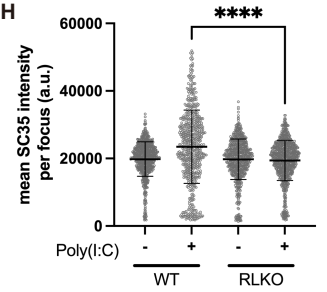
H
****
mean SC35 intensity per focus (a.u.)
60000
40000
20000
0
Poly(I:C)
-
+
-
+
WT
RLKO

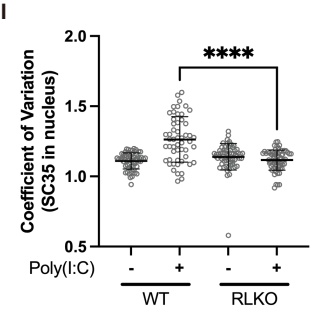
I
****
Coefficient of Variation (SC35 in nucleus)
2.0
1.5
1.0
0.5
Poly(I:C)
-
+
-
+
WT
RLKO

Figure 5

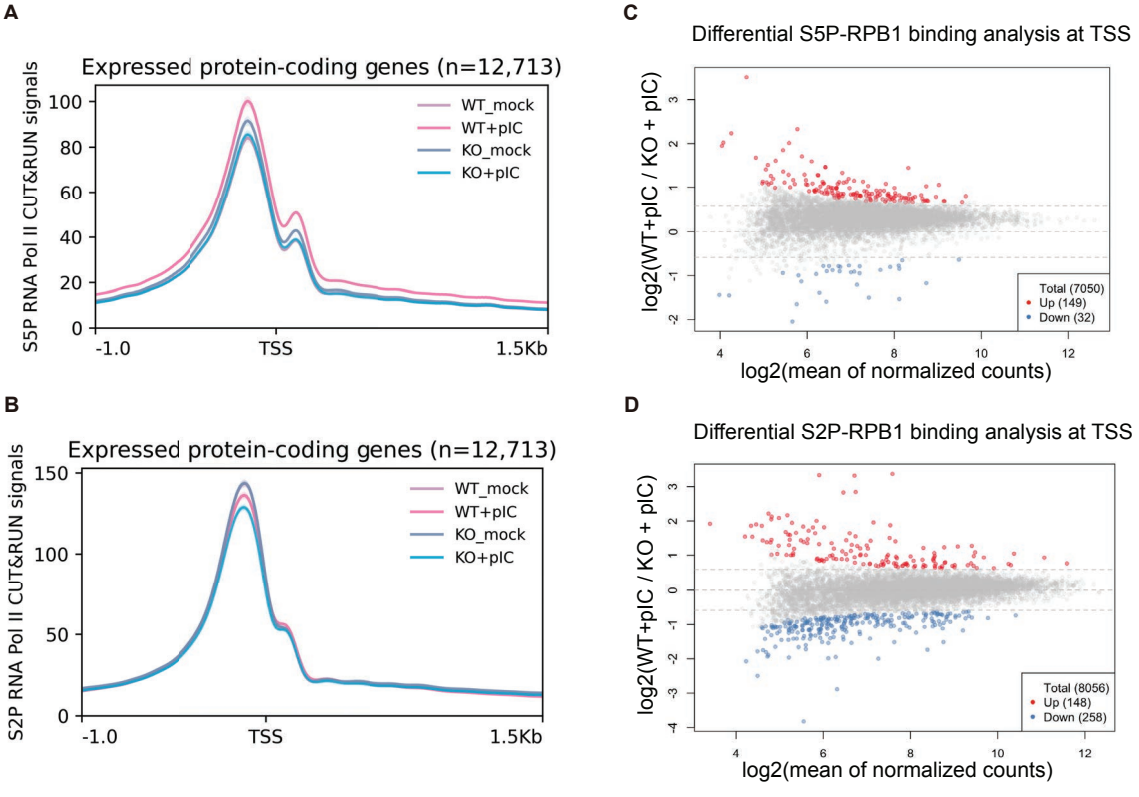
A
Expressed protein-coding genes (n=12,713)
S5P RNA Pol II CUT&RUN signals
WT_mock
WT+pIC
KO_mock
KO+pIC
-1.0
TSS
1.5Kb
B
Expressed protein-coding genes (n=12,713)
S2P RNA Pol II CUT&RUN signals
C
Differential S5P-RPB1 binding analysis at TSS
log2(WT+pIC / KO + pIC)
log2(mean of normalized counts)
Total (7050)
Up (149)
Down (32)
D
Differential S2P-RPB1 binding analysis at TSS
Total (8056)
Up (148)
Down (258)

Figure 6

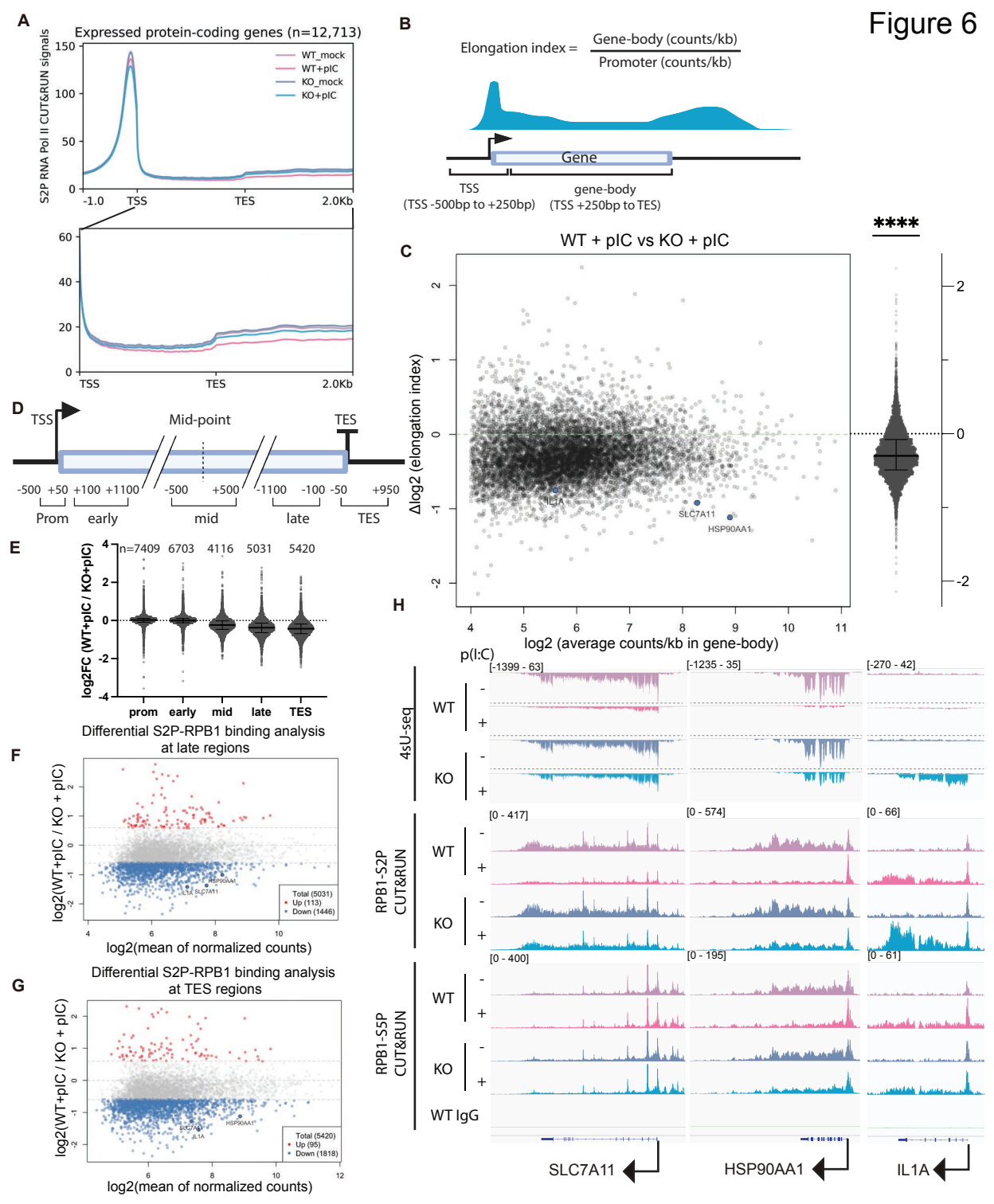
A
Expressed protein-coding genes (n=12,713)
S2P RNA Pol II CUT&RUN signals
WT_mock
WT+pIC
KO_mock
KO+pIC
-1.0
TSS
TES
2.0Kb
B
Elongation index = Gene-body (counts/kb) / Promoter (counts/kb)
Gene
TSS
(TSS -500bp to +250bp)
gene-body
(TSS +250bp to TES)
C
WT + pIC vs KO + pIC
****
Δlog2 (elongation index)
log2 (average counts/kb in gene-body)
IL1A
SLC7A11
HSP90AA1
D
TSS
Mid-point
TES
-500 +50 +100 +1100
-500 +500
-1100 -100
-50 +950
Prom
early
mid
late
TES
E
n=7409 6703 4116 5031 5420
log2FC (WT+pIC / KO+pIC)
prom
early
mid
late
TES
Differential S2P-RPB1 binding analysis at late regions
F
log2(WT+pIC / KO + pIC)
log2(mean of normalized counts)
Total (5031)
Up (113)
Down (1446)
Differential S2P-RPB1 binding analysis at TES regions
G
log2(WT+pIC / KO + pIC)
log2(mean of normalized counts)
Total (5420)
Up (95)
Down (1818)
H
p(I:C)
[-1399 - 63]
[-1235 - 35]
[-270 - 42]
4sU-seq
WT
KO
[0 - 417]
[0 - 574]
[0 - 66]
RPB1-S2P CUT&RUN
[0 - 400]
[0 - 195]
[0 - 61]
RPB1-S5P CUT&RUN
WT IgG
SLC7A11
HSP90AA1
IL1A

Figure 7

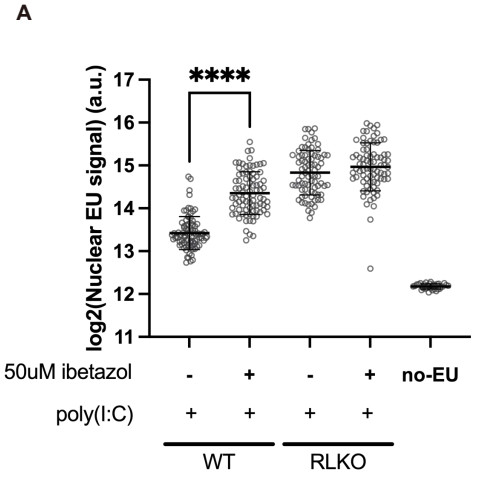
A
log2(Nuclear EU signal) (a.u.)
17
16
15
14
13
12
11
****
50uM ibetazol
-
+
-
+
no-EU
poly(I:C)
+
+
+
+
WT
RLKO

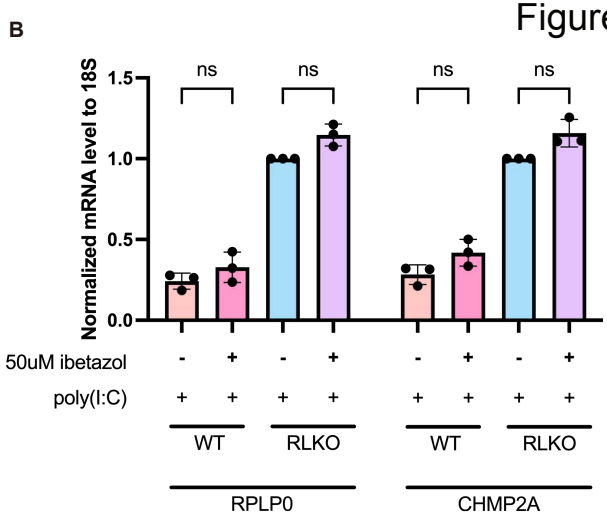
B
Normalized mRNA level to 18S
1.5
1.0
0.5
0.0
ns
ns
ns
ns
50uM ibetazol
poly(I:C)
WT
RLKO
WT
RLKO
RPLP0
CHMP2A

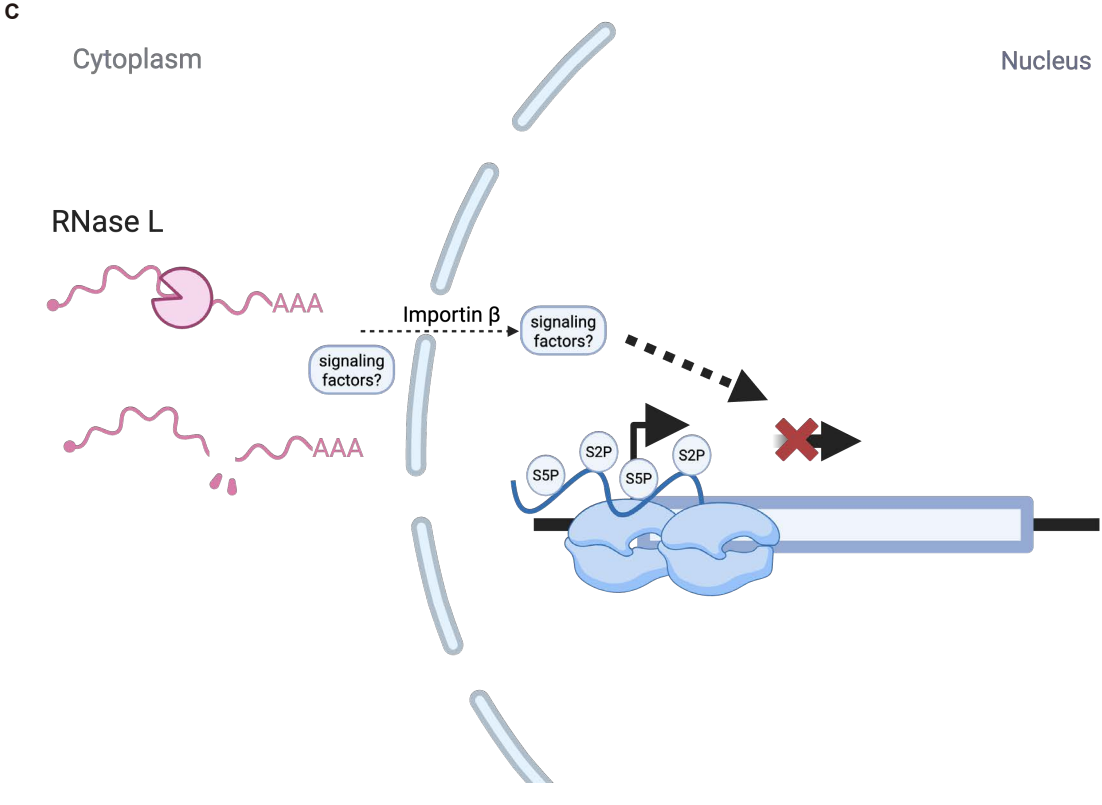
C
Cytoplasm
Nucleus
RNase L
AAA
AAA
Importin β
signaling factors?
signaling factors?
S5P
S2P
S5P
S2P

Figure S1

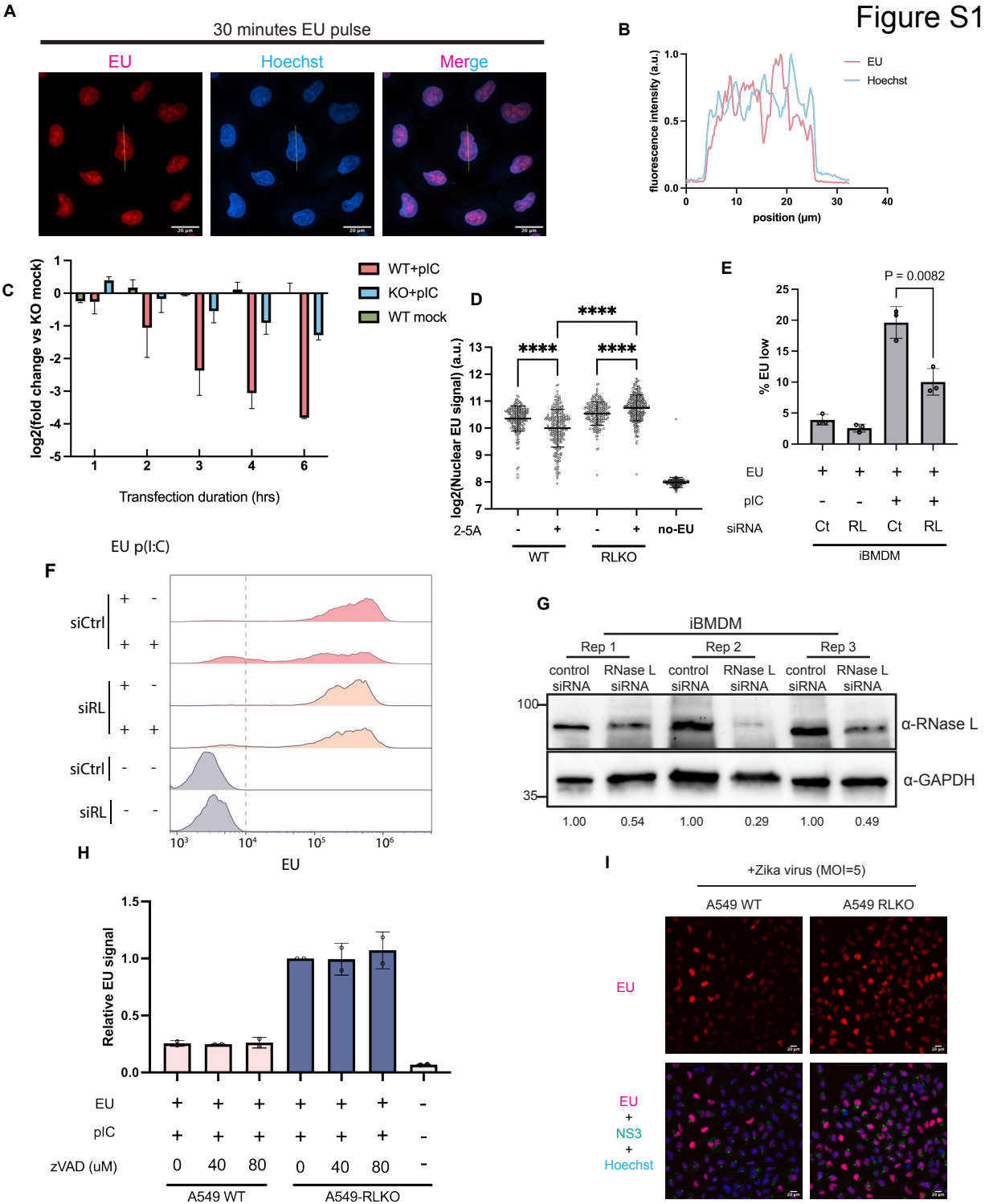
A
30 minutes EU pulse
EU
Hoechst
Merge
B
fluorescence intensity (a.u.)
position (μm)
EU
Hoechst
C
log2(fold change vs KO mock)
Transfection duration (hrs)
WT+pIC
KO+pIC
WT mock
D
log2(Nuclear EU signal) (a.u.)
****
****
****
2-5A
no-EU
WT
RLKO
E
P = 0.0082
% EU low
EU
pIC
siRNA
Ct
RL
Ct
RL
iBMDM
F
EU p(I:C)
siCtrl
siRL
siCtrl
siRL
EU
G
iBMDM
Rep 1
Rep 2
Rep 3
control siRNA
RNase L siRNA
α-RNase L
α-GAPDH
1.00
0.54
1.00
0.29
1.00
0.49
H
Relative EU signal
EU
pIC
zVAD (uM)
A549 WT
A549-RLKO
I
+Zika virus (MOI=5)
A549 WT
A549 RLKO
EU
EU
+
NS3
+
Hoechst

Figure S2

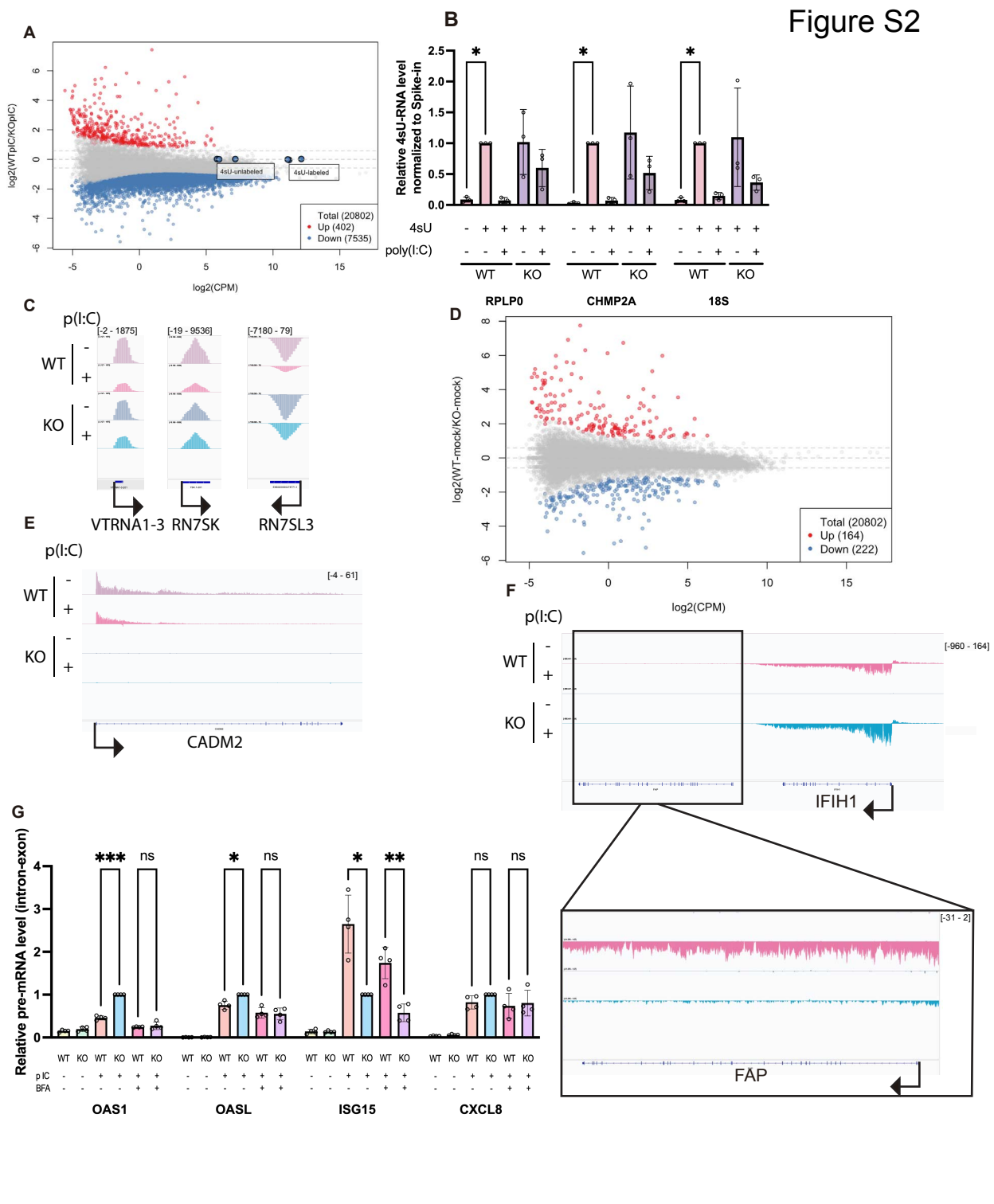
A
log2(WTpIC/KOpIC)
log2(CPM)
4sU-unlabeled
4sU-labeled
Total (20802)
Up (402)
Down (7535)
B
Relative 4sU-RNA level normalized to Spike-in
4sU
poly(I:C)
WT
KO
RPLP0
CHMP2A
18S
C
p(I:C)
WT
KO
[-2 - 1875]
[-19 - 9536]
[-7180 - 79]
VTRNA1-3
RN7SK
RN7SL3
D
log2(WT-mock/KO-mock)
log2(CPM)
Total (20802)
Up (164)
Down (222)
E
p(I:C)
WT
KO
[-4 - 61]
CADM2
F
p(I:C)
WT
KO
[-960 - 164]
IFIH1
[-31 - 2]
FAP
G
Relative pre-mRNA level (intron-exon)
pIC
BFA
OAS1
OASL
ISG15
CXCL8
ns

Figure S3

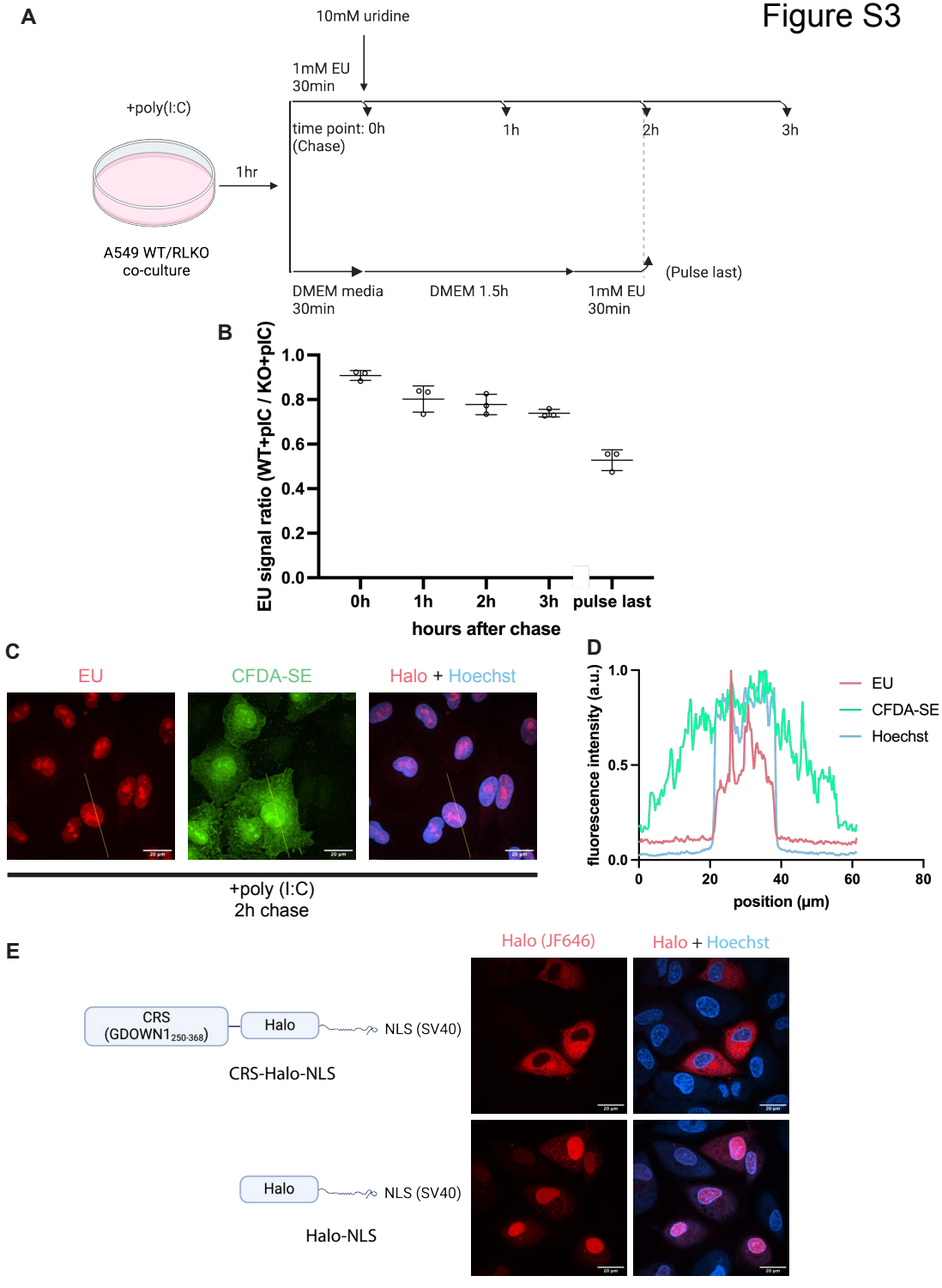
A
10mM uridine
1mM EU
30min
+poly(I:C)
time point: 0h
(Chase)
1h
2h
3h
1hr
A549 WT/RLKO
co-culture
(Pulse last)
DMEM media
30min
DMEM 1.5h
1mM EU
30min
B
EU signal ratio (WT+pIC / KO+pIC)
1.0
0.8
0.6
0.4
0.2
0.0
0h
1h
2h
3h
pulse last
hours after chase
C
EU
CFDA-SE
Halo + Hoechst
+poly (I:C)
2h chase
D
fluorescence intensity (a.u.)
1.0
0.5
0.0
0
20
40
60
80
position (μm)
EU
CFDA-SE
Hoechst
E
Halo (JF646)
Halo + Hoechst
CRS
(GDOWN1250-368)
Halo
NLS (SV40)
CRS-Halo-NLS
Halo
NLS (SV40)
Halo-NLS

Figure S4

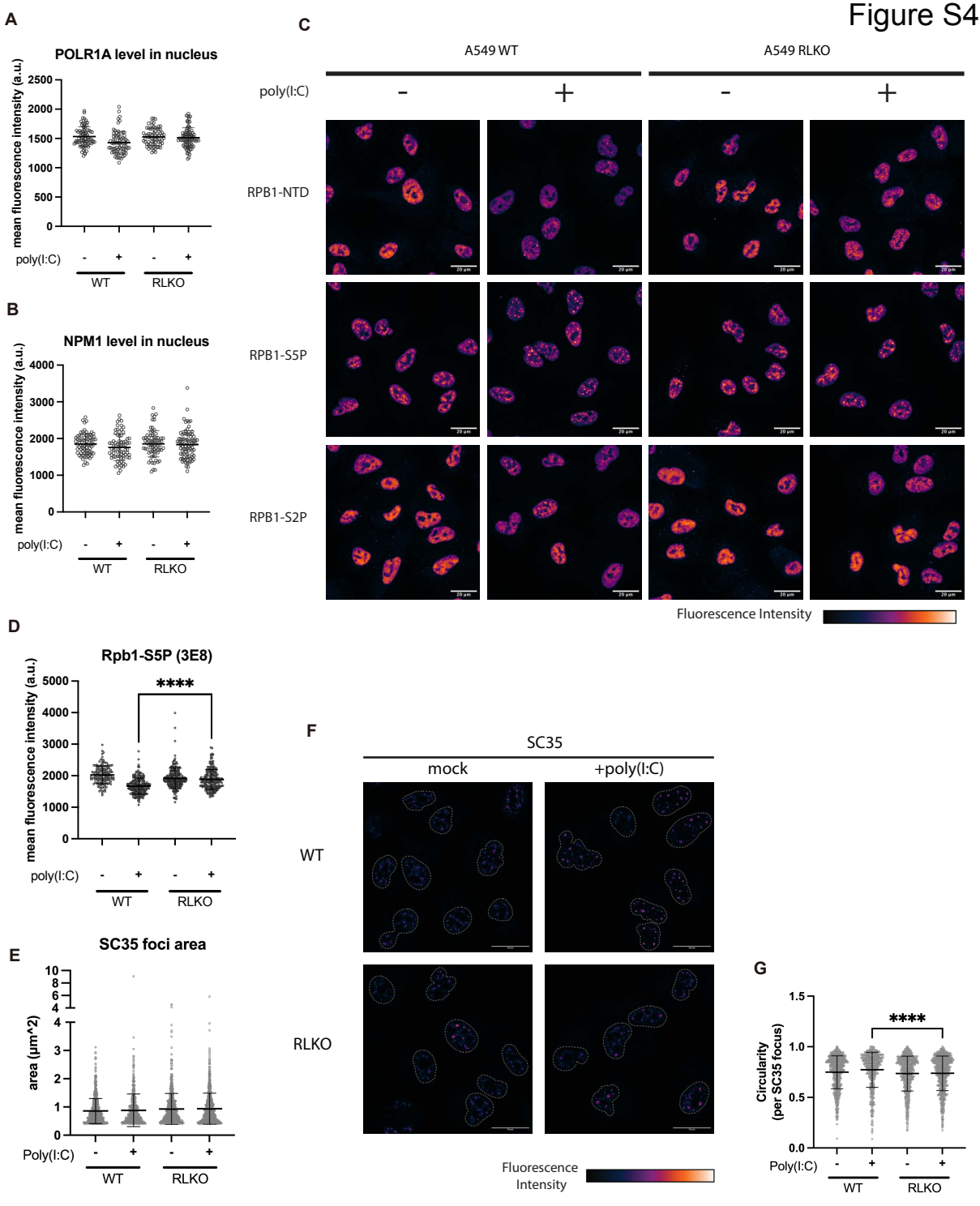
A
POLR1A level in nucleus
mean fluorescence intensity (a.u.)
2500
2000
1500
1000
500
0
poly(I:C)
-
+
-
+
WT
RLKO
B
NPM1 level in nucleus
mean fluorescence intensity (a.u.)
4000
3000
2000
1000
0
poly(I:C)
-
+
-
+
WT
RLKO
C
A549 WT
A549 RLKO
poly(I:C)
-
+
-
+
RPB1-NTD
RPB1-S5P
RPB1-S2P
Fluorescence Intensity
D
Rpb1-S5P (3E8)
****
mean fluorescence intensity (a.u.)
5000
4000
3000
2000
1000
0
poly(I:C)
-
+
-
+
WT
RLKO
E
SC35 foci area
area (µm^2)
10
8
6
4
4
3
2
1
0
Poly(I:C)
-
+
-
+
WT
RLKO
F
SC35
mock
+poly(I:C)
WT
RLKO
Fluorescence Intensity
G
****
Circularity (per SC35 focus)
1.5
1.0
0.5
0.0
Poly(I:C)
-
+
-
+
WT
RLKO

Figure S5

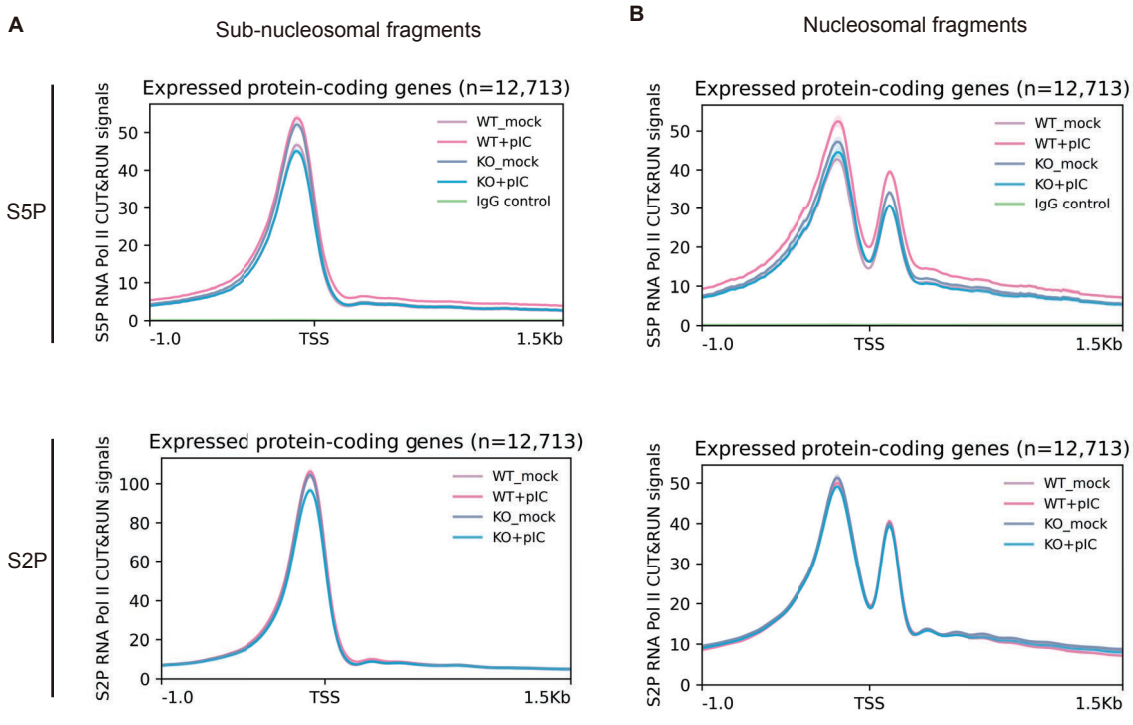
A
Sub-nucleosomal fragments
B
Nucleosomal fragments
S5P
S2P
Expressed protein-coding genes (n=12,713)
S5P RNA Pol II CUT&RUN signals
S2P RNA Pol II CUT&RUN signals
WT_mock
WT+pIC
KO_mock
KO+pIC
IgG control
-1.0
TSS
1.5Kb

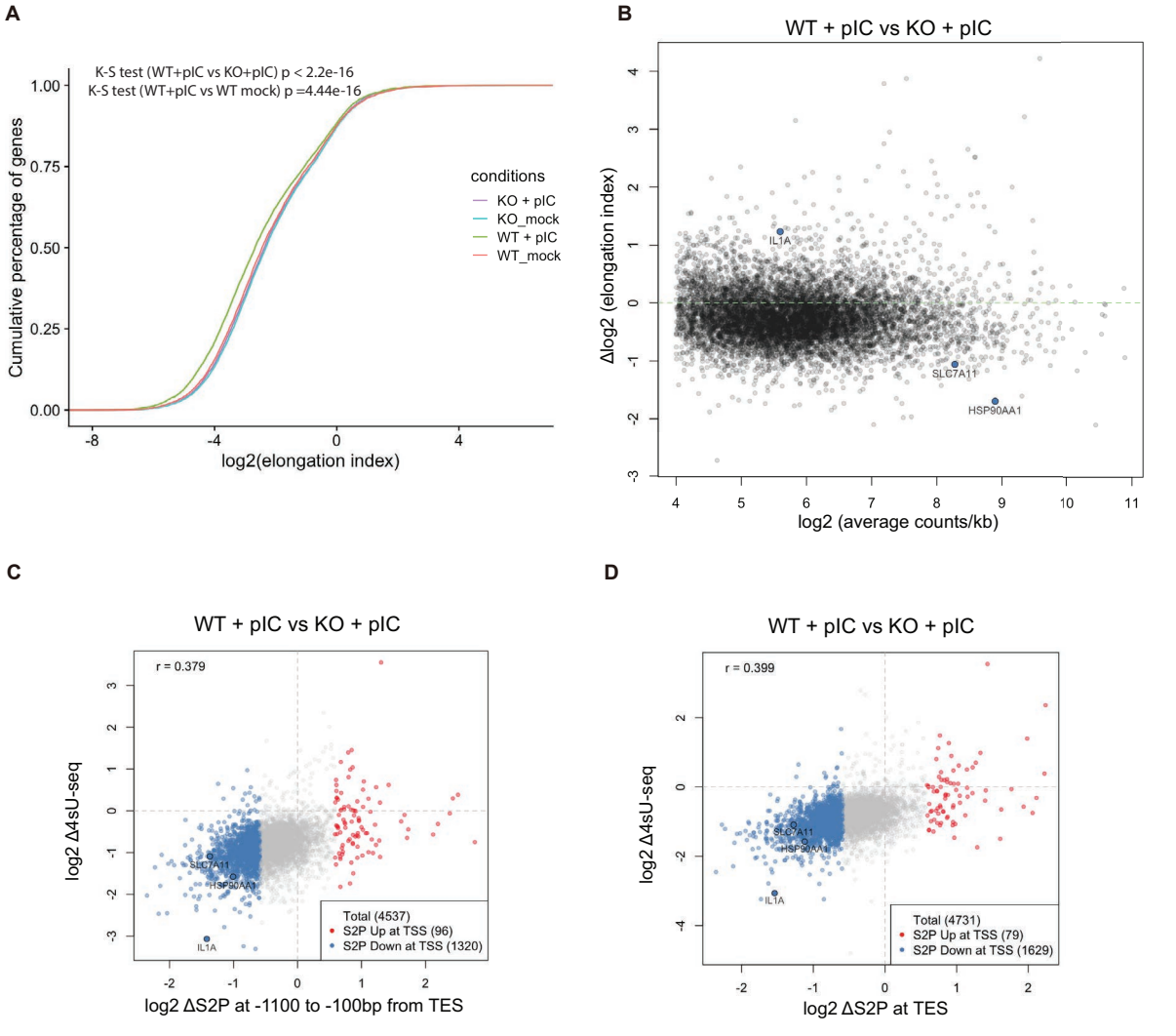
A
K-S test (WT+pIC vs KO+pIC) p < 2.2e-16
K-S test (WT+pIC vs WT mock) p =4.44e-16
Cumulative percentage of genes
log2(elongation index)
conditions
KO + pIC
KO_mock
WT + pIC
WT_mock
B
WT + pIC vs KO + pIC
Δlog2 (elongation index)
log2 (average counts/kb)
IL1A
SLC7A11
HSP90AA1
C
WT + pIC vs KO + pIC
r = 0.379
log2 Δ4sU-seq
log2 ΔS2P at -1100 to -100bp from TES
Total (4537)
S2P Up at TSS (96)
S2P Down at TSS (1320)
D
WT + pIC vs KO + pIC
r = 0.399
log2 Δ4sU-seq
log2 ΔS2P at TES
Total (4731)
S2P Up at TSS (79)
S2P Down at TSS (1629)